M. D.

Enhanced Southern Ocean CO_2 outgassing as a result of stronger and poleward shifted southern hemispheric westerlies

LLaurie C. Menviel[1,2*], P. Paul Spence[2,3], A. Andrew E. Kiss[4,5], M. Matthew A. Chamberlain[3,6], H. Hakase Hayashida[3,7], Matthew H. England[2,8], and Darryn Waugh[9,10]

[1]Climate Change Research Centre, University of New South Wales, Sydney, NSW 2052, Australia
[2]The Australian Centre for Excellence in Antarctic Science, University of New South Wales, Sydney, NSW 2052, Australia
[3]Institute for Marine and Antarctic Studies and Australian Antarctic Program Partnership, University of Tasmania, Hobart, Australia
[4]Research School of Earth Sciences, Australian National University, Canberra, Australia
[5]Australian Research Council Centre of Excellence for Climate Extremes, Australia
[6]CSIRO Oceans and Atmosphere, Hobart, Australia
[7]Application Laboratory, Japan Agency for Marine-Earth Science and Technology, Yokohama, Japan
[8]Centre for Marine Science and Innovation (CMSI), University of New South Wales, Sydney, NSW 2052, Australia
[9]School of Mathematics and Statistics, University of New South Wales, Sydney, NSW 2052, Australia
[10]Dpt. of Earth and Planetary Sciences, John Hopkins University, Baltimore, USA

Correspondence: L. Menviel (l.menviel@unsw.edu.au)

Abstract. While the Southern Ocean (SO) provides the largest oceanic sink of carbon, some observational studies have suggested that the total SO SO total CO_2 (tCO_2) uptake exhibited large (∼0.3 GtC/yr) decadal-scale variability over the last 30 years, with a similar SO COtCO$_2$ uptake in 2016 than as in the early 1990s. Here, using an eddy-rich ocean, sea-ice, carbon cycle model, with a nominal resolution of $1/10^{th}$ degree0.1°, we explore the changes in total, natural and anthropogenic SO CO_2 fluxes in the Southern Ocean over the period 1970-2021 1980-2021 and the processes leading to the CO_2 flux variability. The simulated total COtCO$_2$ flux exhibits decadal-scale variability with an amplitude of ∼0.1 GtC/yr globally in phase with observationsand with variability in the Southern Annular Mode (SAM). Notably, a stagnation of the total COtwo stagnation in tCO$_2$ uptake is are simulated between 1982 and 2000 as well as since 2012, while a re-invigoration is simulated between 2000 and 2012. This decadal-scale variability results from enhanced outgassing of is primarily due to changes in natural CO_2 (nCO_2) fluxes south of the sub-Antarctic front due to the strengthening and poleward shift of the polar front associated with variability in the Southern Annular Mode (SAM). Positive phases of the SAM, i.e. stronger and poleward shifted southern hemispheric (SH) westerlies. Changes in SO CO, lead to enhanced SO nCO$_2$ fluxes can be mostly explained by variations in surface outgassing due to higher surface natural dissolved inorganic carbon (DIC) brought about by a combination of Ekman-driven vertical advection and DIC diffusion at the base of the mixed layer. The pattern of the CO_2 flux anomalies indicate a dominant control of the interaction between the mean flow south of the polar front and the main topographic features.These wind changes While positive phases of the SAM also lead to enhanced anthropogenic CO_2 (aCO_2) uptake south of the polar front, even though the correlation is low and the amplitude 75% smaller than for the natural COthe amplitude of the changes in aCO$_2$ changes. The total SO COfluxes is only 25% of the changes in nCO$_2$ fluxes. Due to the larger nCO$_2$ outgassing

compared to aCO_2 uptake as the SH westerlies strengthen and shift poleward, the SO tCO_2 uptake capability thus reduced since ~~1970~~ 1980 in response to ~~a~~ the shift towards positive phases of the SAM. Our results indicate that, even in an eddy-rich ocean model, a strengthening and/or poleward shift of the ~~southern hemispheric~~ SH westerlies enhance CO_2 outgassing. The projected poleward strengthening of the SH westerlies over the coming century will thus reduce the capability of the SO to mitigate the increase in atmospheric CO_2.

1 Introduction

As a result of anthropogenic emissions of greenhouse gases, atmospheric CO_2 concentration (CO_{2atm}) increased from a natural level of 277 ppm in 1750 (Joos and Spahni, 2008) to 415 ppm in 2021 (Friedlingstein et al., 2022). The terrestrial biosphere and the ocean have however strongly mitigated the anthropogenic emissions of carbon, respectively absorbing ∼31% and 24% of the emissions (Le Quéré et al., 2018). The largest oceanic carbon sink is the Southern Ocean (SO), which has contributed ∼40% of the global oceanic CO_2 uptake in the 1990s (Sabine et al., 2004; Mikaloff-Fletcher et al., 2006). In the context of continued ~~sustained~~ anthropogenic emissions of greenhouse gases, ~~a better understanding of~~ it is crucial to better understand the impact of climate change on ~~the ocean uptake of anthropogenic CO_2 (aCO_2), but also on the~~ atmosphere-ocean total (sum of anthropogenic and natural) CO_2 (tCO_2) fluxes~~between the ocean and the atmosphere is needed.~~.

There is evidence for large decadal variability in the total SO carbon uptake ~~(LeQuéré et al., 2007; Matear and Lenton, 2008; Landschütz~~ Observational estimates, covering the period 1982-2011, suggest the total carbon uptake in SO was lower than expected in the 1990s, but increased significantly between 2002 and 2011 to reach a maximum of 1.2 ~~PgC~~ GtC yr^{-1} in 2011 (LeQuéré et al., 2007; Landschützer et al., 2015; Gruber et al., 2019b). Between 2011 and 2016, observational estimates combining the Surface Ocean CO_2 ATlas (SOCAT) and Southern Ocean Carbon and Climate Observations and Modeling (SOCCOM) suggest that the SO tCO_2 uptake weakened ~~again (Bushinsky et al., 2019; Gruber et al., 2019b; Keppler and Landschützer, 2019)~~by ∼0.4 GtC yr^{-1} (Bushinsky et al., 2019; Gruber et al., 2019b; Keppler and Landschützer, 2019), while observational estimates only including SOCAT suggest the tCO_2 uptake stabilised between 2011 and 2016, and increased since 2017 (Landschützer et al., 2020). There is ~~, however,~~ significant uncertainty associated with these estimates due to the sparsity of the data, particularly in the 1990s ~~(Ritter et al., 2017)~~(Ritter et al., 2017; Gregor et al., 2018), and little information prior to 1982. In addition, this data scarcity might lead to a 39% overestimation of the amplitude of SO decadal tCO_2 uptake variability (Gloege et al., 2021).

The SO circulation is mostly driven by SH westerly winds, which generate an equatorward Ekman transport and an associated upwelling of carbon-rich deep waters. Changes in the position and strength of the SH westerlies are linked to the dominant mode of atmospheric variability in the southern hemisphere, the SAM. Positive SAM phases, which are associated with poleward contraction and stronger than average westerly winds, have been observed between 1979 and 2000, particularly during austral summer and autumn (Thompson and Solomon, 2002; Fogt and Marshall, 2020). This intensification and poleward shift of the SH westerlies result from stratospheric ozone depletion and an increase in greenhouse gases (Arblaster and Meehl, 2006). However, due to stratospheric ozone recovery, a pause in the poleward intensification of the SH westerlies has ~~recently been observed (Banerjee et al., 2020).~~ been observed between 2000 and ∼2010 (Banerjee et al., 2020). The SAM

trend is however positive since ~2010. The continued increase in greenhouse gases is taking over the ozone impact and is suggested to result in a long-term positive SAM trend over the 21st century (Thompson et al., 2011).

Numerical studies have highlighted the role of SH westerlies in modulating the upwelling of DIC-rich deep water and thus the carbon exchange between the atmosphere and the ocean. Stronger SH westerlies enhance the SO upwelling, leading to an oceanic loss of carbon and thus an increase in CO_{2atm} (Toggweiler, 1999; Lauderdale et al., 2013; Lovenduski et al., 2007, 2008; Munday et al., 2014; Lauderdale et al., 2017; Menviel et al., 2018). Changes in the strength and position of the SH westerlies associated with the SAM could thus significantly modulate interannual SO CO_2 fluxes (Resplandy et al., 2015). The increase in surface ~~Dissolved Inorganic Carbon (DIC)~~ DIC as a result of stronger SO upwelling could however be partly mitigated by enhanced export production at the surface of the SO (Menviel et al., 2008; Hauck et al., 2013). In addition, the impact of latitudinal changes in the position of the SH westerlies on oceanic carbon and CO_{2atm} is uncertain as it might depend on the initial position of the SH westerlies and on how the latitudinal ~~change~~ changes in the SH westerlies ~~impacts~~ impact the oceanic circulation (Völker and Köhler, 2013; Lauderdale et al., 2013, 2017).

Most of the numerical studies analysing the impact of SH westerly changes mentioned above focused on natural carbon. Given the increase in anthropogenic carbon emissions since 1870, the natural carbon cycle has been perturbed, and the impact of changes in the strength and position of the SH westerly winds on anthropogenic carbon uptake also needs to be taken into account. Only a few studies performed with coarse resolution ocean models (Lovenduski et al., 2007, 2008) have assessed the impact of the SAM on total, anthropogenic and natural CO_2 fluxes. They found that positive phases of the SAM led to an outgassing of natural CO_2 (nCO_2), while enhancing the uptake of aCO_2, with the net effect being a reduction in the tCO_2 uptake. Lenton and Matear (2007) also simulated a reduction in tCO_2 uptake in response to the SAM but did not ~~deconvolve~~ distinguish between the natural and anthropogenic contributions.

Some studies have thus attributed the weaker SO carbon uptake observed in the 1990s to a positive trend in the ~~Southern Annular Mode (SAM) (Marshall, 2003; LeQuéré et al., 2007; Lenton and Matear, 2007; Lovenduski et al., 2007, 2008).~~ SAM (Marshall, 2003; LeQuéré et al., 2007; Lenton and Matear, 2007; Lovenduski et al., 2007, 2008; Gruber et al., 2023). This is supported by recent observations-based studies, which concluded that the multi-decadal surface SO pCO_2 variability, particularly the winter trend, was driven by the SAM (Gregor et al., 2018; Nevison et al., 2020), even though it was also suggested that on top of this multi-decadal trend net primary production could affect interannual variability (Gregor et al., 2018). On the other hand, McKinley et al. (2020) suggested that the lower 1990s CO_2 uptake was a response to the slower CO_{2atm} growth rate.

Regarding, the re-invigoration of the SO carbon uptake in the 2000s, Landschützer et al. (2015) suggested that it could not be attributed to the SAM because the ERA-interim reanalysis did not display the associated wind changes. Instead, they attributed the enhanced carbon uptake to increased solubility in the Pacific sector of the SO due to surface cooling, and a weaker upwelling of DIC-rich waters in the Atlantic and Indian sectors of the SO. More recently, by analysing changes in SO tCO_2 fluxes between 1980 and 2016, Keppler and Landschützer (2019) suggested that the net effect of the SAM on tCO_2 uptake was nil and that instead the variability was arising from regional shifts in ~~surface~~ SO surface air pressure linked to zonal wavenumber 3.

~~Thus there are~~ There are thus uncertainties not only in the magnitude of the decadal variability but also on the processes controlling SO carbon uptake, and there is a need for further studies examining these issues. In addition, ~~there is a need to include~~ the impacts of mesoscale eddy activity on the SO oceanic circulation and transport of nutrient and carbon needs to be better constrained. The prevalent mesoscale eddy activity in the SO significantly influences heat, salt and nutrient transport as well as the SO lateral and meridional overturning circulations. Mesoscale eddy transports generally act in the opposite sense to the wind driven transport in the SO, and thus the response of the ocean circulation to changes in the winds varies across model studies. For example, a doubling of the magnitude of SH westerly winds doubles the simulated circumpolar transport in coarse resolution models that poorly parameterize eddies, but this doubling does not occur in eddy-resolving simulations (Hallberg and Gnanadesikan, 2006; Farneti et al., 2010; Spence et al., 2010; Dufour et al., 2012; Morrison and Hogg, 2013; Munday et al., 2013). Further, Dufour et al. (2013) showed in an eddy-permitting ($\sim$0.5° resolution) model that even though a strengthening and poleward shift of the SH westerlies, representing positive phases of the SAM, leads to stronger Ekman-induced northward natural DIC transport, a third of this is compensated by enhanced southward natural DIC transport through eddies. Dufour et al. (2013) also suggested that the higher surface DIC during positive phases of the SAM resulted from enhanced vertical diffusion at the base of the mixed layer and not from vertical advection.

Here, we analyze a simulation ~~run over the period 1970-2021~~ of the period 1980-2021 performed with an eddy-rich ocean, sea ice, biogeochemical model and forced with the 55-year Japanese Reanalysis for driving oceans (JRA55-do) (Tsujino et al., 2018) atmospheric fields to better understand the interannual to multi-decadal variability in SO natural, anthropogenic and total CO_2 fluxes and their links to changes in the SAM.

2 Methods

2.1 Models

Changes in SO carbon uptake are examined using a simulation performed with the eddy-rich ACCESS-OM2-01 global model configuration run under interannual forcing ~~during 1970-2021.~~ between 1958 and 2021. The ocean model is the Modular Ocean Model (MOM) version 5.1 (Griffies, 2012) with a nominal resolution of 0.1° and 75 vertical levels increasing smoothly in thickness from 1.1 m at the surface to 198.4 m at the bottom (5808.7 m depth). The ocean model is coupled to the thermodynamic-dynamic Los Alamos sea-ice model (CICE) version 5.1.2 (Hunke et al., 2017). ACCESS-OM2 is described in detail in Kiss et al. (2020), but the version presented here has many improvements ~~, including ocean biogeochemistry with two-way coupling to nutrient and algae carried in the sea ice model (Hayashida et al., 2021)~~as described in Solodoch et al. (2022). The main improvements are that the wind stress calculation now uses relative velocity over both ocean and sea ice (not just ocean), and the albedo of the ocean is now latitude-dependent following Large and Yeager (2009).

The ocean biogeochemical model is the Nutrient-Phytoplankton-Zooplankton-Detritus (NPZD) model WOMBAT (Whole Ocean Model of Biogeochemistry And Trophic-dynamics) (Kidston et al., 2011; Oke et al., 2013; Law et al., 2017). WOMBAT includes DIC, $CaCO_3$, alkalinity, oxygen, phosphate and iron, that are linked to the phosphate uptake and remineralisation through a constant Redfield ratio. The biogeochemical parameters are identical to those of the ACCESS-ESM1.5 model (Ziehn

et al., 2020), apart from the pre-industrial CO_{2atm} value. Two DIC tracers are included, a natural DIC (nDIC) and a total DIC (tDIC), with the difference between the two providing an estimate of anthropogenic DIC (aDIC). nDIC exchanges carbon with a constant pre-industrial CO_{2atm} concentration of 284.32 ppm, whereas tDIC exchanges carbon with the time evolving, observed CO_{2atm}, which includes the current increase due to anthropogenic emissions. For the tDIC tracer, the CO_{2atm} concentration is spatially uniform and annually-averaged, and follows the Ocean Model Intercomparison Project (OMIP) protocol until 2014 (Orr et al., 2017) and NOAA GML data thereafter, rising from 315.34 ppm in 1958 to 339.7 ppm in 1980 and 414.72 ppm in 2021 ~~, with an average rate of increase of 1.56 ppm/yr~~ (Fig. ~~??~~2a). The air-sea CO_2 exchange is a function of the difference in partial pressure of CO_2 at the air-sea interface, the wind speed (Wanninkhof, 1992) and sea ice concentration. This version also includes a two-way coupling of the ocean biogeochemistry with nutrient and algae carried in the sea ice model (Hayashida et al., 2021). Note, physical and biogeochemical changes in the ocean simulations do not impact the atmospheric state, and in all simulations the longwave radiative forcing is given by the evolving JRA55-do fields over 1970-2021. Biogeochemical tracers also have no effect on the ocean or sea ice physical state (including shortwave penetration depth), and oxygen has no effect on other biogeochemical tracers.

2.2 Simulations

The model is forced by atmospheric conditions taken from the 55-year Japanese Reanalysis for driving oceans (JRA55-do) version 1.4, 1.5.0 and 1.5.0.1 (Tsujino et al., 2018), that now covers the period 1958 to 2021. JRA55-do ~~provides~~ allows calculation of air-sea fluxes of momentum, heat and freshwater at a 3 hourly time interval and with a horizontal resolution of 0.5625°. The model is forced by four 61-year cycles of JRA55-do v1.4 for the period 1958-2018. In cycle 1, the ocean model was initialised with modern-day temperature and salinity distributions derived from the World Ocean Atlas 2013 version 2 (Locarnini et al., 2013). Subsequent cycles used the final state of the previous cycle as the initial condition, and proceeded through another JRA55-do v1.4 1958-2018 forcing cycle. Cycles 1–3 do not include biogeochemistry.

Here we analyse cycle 4, which includes WOMBAT BGC and has also been extended from 2019 until the end of 2021 using JRA55-do v1.5.0 for 2019 and JRA55-do v1.5.0.1 thereafter. Ocean and ice physical fields were initialised from the values at the end of cycle 3. Biogeochemical fields other than oxygen were initialised at the start of cycle 4 (1958). A uniform 0.01 mmol m^{-3} initial value was used for phytoplankton, zooplankton, detritus and $CaCO_3$. Initial alkalinity, tDIC and nDIC were interpolated from a 305 years-long spinup run at 1 degree resolution (i.e., the first 5 cycles of OMIP2~~(Mackallah et al., 2022))~~) (Mackallah et al., 2022). GLODAPv2 (Olsen et al., 2016) was used to initialise phosphate, and iron was initialised from the FEMIP median value (Tagliabue et al., 2016). Oxygen was initialised from GLODAPv2 at 1 Jan 1979 due to a configuration mistake; this has no effect on other variables. Initial phosphate and algae in the bottom 3 cm of sea ice were set to zero, but quickly equilibrate with those in the surface ocean layer. The physical state of the ACCESS-OM2-01 global model is consistently simulated across all four, 61-year forcing cycles. Here, we skip the first ~~twelve~~ 22 years of the fourth cycle (i.e. ~~1958-1970~~1958-1980) from our analysis to allow the simulation to recover from the reset at the end of the previous cycle, and focus our analysis on the period 1980-2021, following phase II of the Coordinated Ocean-ice Reference Experiments (CORE).

To better assess the impact of high model resolution, we also provide a comparison with the results of a 1° resolution configuration of ACCESS-OM2. This is based on that described by Kiss et al. (2020), but is forced with the newer JRA55-do v1.4 1958–2018 dataset and includes WOMBAT biogeochemistry. Specifically, this simulation corresponds to the final (6^{th}) cycle of omip2-spunup (Mackallah et al., 2022) after 33 cycles were performed as spin-up. Similar to ACCESS-OM2-01, in the version of ACCESS-OM2 used here the wind stress calculation uses relative velocity over both ocean and sea ice and the albedo of the ocean is latitude-dependent following Large and Yeager (2009). The 1° configuration has flow-dependent Gent and McWilliams (1990) parameterisation of unresolved mesoscale eddies, as described in Kiss et al. (2020).

2.3 Analysis

For consistency with the forcing, the SAM index is calculated from the JRA55-do dataset with the methodology described in Stewart et al. (2020). The SAM index as calculated from the JRA55-do dataset captures well the SAM index based on observations (Marshall, 2003; Stewart et al., 2020).

In this study the SO polar front (PF) and ~~subantarctic~~ sub-Antarctic front (SAF) are defined as the 1.2°C annual minimum surface temperature contour, and 4°C isotherm at 400m depth, respectively following the definition of Sokolov and Rintoul (2009). Their simulated zonal mean latitude locations are 56.3°S and 48.2°S, respectively.

~~To better understand the drivers of changes in ocean-atmosphere CO_2 fluxes, changes in natural surface water~~ Oceanic natural pCO_2 ~~are decomposed into their~~ is a function of nDIC, alkalinity (ALK) ~~and solubility (sea surface salinity, SSS and sea surface temperature , SST) contributions in the following way (Sarmiento and Gruber, 2006):~~ as well as ocean temperature (T) and salinity (Sal). Changes in pCO_2 can thus be described as:

$$\Delta pCO_2 = \frac{\partial(pCO_2)}{\partial(DIC)}.\Delta DIC + \frac{\partial(pCO_2)}{\partial(ALK)}.\Delta ALK + \frac{\partial(pCO_2)}{\partial(Sal)}.\Delta Sal + \frac{\partial(pCO_2)}{\partial(T)}.\Delta T \quad (1)$$

To better understand the processes leading to surface ocean pCO_2 changes, we can estimate the pCO_2 change from each of the above variables separately. Broecker et al. (1979) derived that if ALK, salinity and temperature are constant then:

$$\frac{\partial ln(pCO_2)}{\partial ln(DIC)} = \gamma DIC \quad (2)$$

with γDIC being the Revelle factor of DIC.

Equation 1 can be re-written as:

$$\Delta pCO_2 \frac{DIC}{pCO_2}.\frac{\partial pCO_2}{\partial DIC} = \Delta pCO_{2DIC} + \Delta pCO_{2ALK} + \Delta pCO_{2SSS} + \Delta pCO_{2SST}\gamma DIC \quad (3)$$

~~The DIC , ALK and SSS contributions to~~ One can then derived the pCO_2 change due to a change in DIC (ΔpCO_{2DIC}) as:

$$\Delta pCO_{2DIC} = \gamma_{DIC} pCO_2 \frac{\Delta DIC}{DIC} \quad (4)$$

Here we use a mean high latitude estimate for γ_{DIC} of 13.3 (Sarmiento and Gruber, 2006) to estimate pCO_{2DIC}. pCO_2 ~~are of the form~~ sensitivities to ALK and salinity can be derived with similar equations:

$$\Delta pCO_{2ALK} = \gamma_{ALK} pCO_2 \frac{\Delta ALK}{ALK} \quad (5)$$

and

$$\Delta pCO_{2Sal} = \gamma_{Sal} pCO_2 \frac{\Delta Sal}{Sal} \quad (6)$$

with $\gamma_{ALK} = -12.6$ and $\gamma_{Sal} = 1$ (Sarmiento and Gruber, 2006).

Finally, Takahashi et al. (1993) suggest that the pCO_2 sensitivity to temperature (T) follows the relationship:

$$\Delta pCO_{2X} \frac{\partial ln(pCO_2)}{\partial T} = \gamma_X \Delta X/, 0.0423^\circ C^{-1} \quad (7)$$

~~where $\overline{pCO_2}$ is the surface~~

This implies (Takahashi et al., 2002, 2009) that the change in pCO_2 ~~averaged over the years 1980-1982 and $\overline{X}$ represents the surface DIC, ALK or SSS, also averaged over 1980-1982. Here $\gamma_{DIC} = 13.3$ is the high-latitude Revelle factor, $\gamma_{ALK} = -12.6$ is the high-latitude sensitivity factor and $\gamma_{SSS} = 1$.~~ due to temperature is:

$$\Delta pCO_{2T} = (e^{0.0423\Delta T} - 1) pCO_2 \quad . \quad (8)$$

~~The SST contribution is given by~~

$$\Delta pCO_{2SST} = (e^{\gamma_{SST}\Delta SST} - 1)\overline{pCO_2}$$

~~where γ_{SST} is equal to 0.0423~~Changes in oceanic remineralised carbon concentration (C*org*) between 1980 and 2021 are estimated as follows:

$$\Delta Corg = R_{C/P} \Delta PO_{4Reg} \quad (9)$$

with

$$\Delta PO_{4Reg} = R_{P/O2} \Delta AOU \quad (10)$$

AOU is the apparent oxygen utilisation, and is the difference between the dissolved oxygen at saturation (as a function of temperature and salinity) and the simulated dissolved oxygen concentration. $R_{C/P}$ and $R_{P/O2}$ are the Redfield ratios equal to 106/~~K~~1 and 1/172, respectively.

3 Results

3.1 Mean CO_2 flux patterns

Performances Performance of the multi-resolution ACCESS-OM2 model suite are is discussed in Kiss et al. (2020). The eddy-rich ACCESS-OM2-01 model at 0.1° resolution provides a reasonable and consistent representation of the state of the ocean, with a particularly good representation of the oceanic SO circulation structure, dense shelf water formation and abyssal overturning cell (Morrison et al., 2020). The simulated horizontal and vertical gradients in tDIC, alkalinity and dissolved oxygen (O_2) in the Southern Ocean are in good agreement with observations (Olsen et al., 2016) (Fig. S1). The absolute values of tDIC and alkalinity are $\sim$60 μmol/kg^{-1} lower than those estimated by GLODAP. This bias might lead to a $\sim$ 10-15 ppm underestimation of the total pCO_2 of SO waters, which can explain the slight overestimation of the does not seem to significantly impact the SO tCO_2 uptake as detailed below.

The mean SO tCO_2, nCOThe concentrations of the different biogeochemical tracers are not constant through the simulation since the atmospheric forcing varies (among other reasons), however the trends averaged over the Southern Ocean and at different depths are much lower than 1% (Fig. S2). In addition, apart from the nDIC at intermediate depth and dissolved O_2 and aCO_2 fluxes averaged over years 1982-2021 are shown in figure 1. at depth, the trends are similar in the 0.1° and 1° resolution, even though the 1° resolution has been equilibrated for a longer time. This indicates that both the 0.1° and 1° simulations can be used to study the SO biogeochemical response to the atmospheric forcing.

We first assess the performance of the model by comparing the time-mean simulated SO tCO_2 fluxes can be compared to observational estimates derived from the self-organizing map-feed-forward (Fig. 1a,b). The SOCAT version 6 (Bakker et al., 2016) provides surface ocean CO_2 measurements. However, due to the spatial and temporal heterogeneity of these measurements, it does not provide an appropriate dataset for a comparison with simulated fields. To fill this gap, Landschützer et al. (2016) developed a method to provide a global gridded monthly observational estimate. The ocean is first clustered into biogeochemical provinces using Self-Organizing Map (SOM). Then, within each biogeochemical province, pCO_2 estimates are generated based on a non-linear relationship between the SOCATv6 observations and the CO_2 driver variables through a feed-forward neural network (SOM-FFN) dataset (Landschützer et al., 2015) and from autonomous biogeochemical floats (Gray et al., 2018; Prend et al., 2022). When averaged over years FFN) approach. If averaged over the available period of 1982-2021, the SO is a net sink of observationally-derived SOM-FFN dataset (Landschützer et al., 2020) (Fig. 1a) displays a strong tCO_2 uptake north of 50°S (-1.59 mol/m^2/yr, zonal average between 50°S and 35°S), and a weak tCO_2 with a strong uptake simulated north of uptake (-0.38 mol/m^2/yr) south of 50°S, even though there are some areas with outgassing ($\sim$0.2 mol/m^2/yr) south of 50°S.

These features are relatively well reproduced by the simulated tCO_2 fluxes (Fig. 1b), which display a similar strong uptake (-1.59 mol/m^2/yr) north of 50°S, that is generally north of the SAF (Sokolov and Rintoul, 2009), in agreement with observations. Some areas however display an outgassing of . As in the observations, some tCO_2 , mostly outgassing ($\sim$0.4 mol/m^2/yr) is simulated south of the PF, but also between the SAF and the PF in parts of the Atlantic and Indian sectors. Observational estimates also suggest moderate SAF, but particularly south of the PF. While both observational estimates and simulation suggest a tCO_2 outgassing south of the PF . Overall, the average SO at 0 – 60°E, 150°E – 180°E, and downstream of the Drake

passage, the simulated tCO_2 ~~uptake is 0.37 GtC/yr higher in the simulation than the observational estimates. When zonally integrated,~~ outgassing is particularly confined to some hotspots, namely over the eastern part of the Southeast Indian Ridge, east of Drake Passage and over the Southwest Indian Ridge (Fig. 1b). Overall, a similarly weak tCO_2 ~~fluxes are small~~ uptake (-0.59 mol/m^2/yr) is estimated south of 50°S~~and the ocean uptake peaks at about 40°S (Fig. S2e).~~ .

These fluxes can be decomposed into their nCO_2 and aCO_2 components, thus highlighting an uptake of aCO_2 nearly everywhere south of 35°S (Fig. 1d), with ~~a maximum south of the PF (~56.3~~two zonally-averaged maximum aCO_2 uptake at 42°S ~~, Fig. S2d).~~ and 55°S (Fig. S3f). While this is broadly consistent with observational estimates, the observations suggest a maximum aCO_2 uptake at 50°S (Gruber et al., 2023). By contrast, an outgassing of nCO_2 is simulated south of the PF and in the frontal zone of the Indian sector (~~Fig~~Figs. 1c ~~). While the simulated nCO_2 outgassing is very localized during 1980-1984, it is in the order of 0.1 x 10^8 molC/m/yr since the late 1990s (Fig. S2c).~~ and S3e).

The upwelling of DIC-rich deep waters south of the PF (Figs. 1e and ~~S2b~~S3c) and the subsequent northward advection of these waters (Fig. S3b) contribute to the nCO_2 outgassing south of 50°S. Through Ekman transport, surface waters in the SO move equatorward (Fig. S3b), and nutrients and DIC are consumed by phytoplankton, leading to a maximum detritus flux at ~42°S (Fig. S3d) and nCO_2 ocean uptake north of the SAF (Fig. S3e), where Antarctic Intermediate Waters (AAIW) and Subantarctic Mode Waters (SAMW) are formed. Within the model framework, the detritus flux at 100m depth provides an estimate of export production.

The pattern of mean simulated SO CO_2 fluxes are similar in the 0.1° (ACCESS-OM2-01) and 1° (ACCESS-OM2) version of the model (Figs. S3 and S4), implying a dominant effect of the large-scale oceanic circulation on the CO_2 fluxes. The main differences are that the tCO_2, nCO_2 and aCO_2 flux hotspots over the eastern part of the Southeast Indian Ridge, east of the Drake Passage and over the Southwest Indian Ridge are more pronounced in the ACCESS-OM2-01 (Fig. 1b,c,d) than in the ACCESS-OM2 (Fig. S4b,c,d), implying a stronger interaction between circulation and topography in the eddy-rich model.

3.2 Temporal changes in CO_2 fluxes

We now look at the time evolution of SO CO_2 fluxes since ~~1970~~ 1980 (Fig. ~~??~~2). From ~~1970~~ 1980 to 2021, the SO nCO_2 uptake (Fig. ~~??~~2c, grey and shading) reduces by ~~0.25~~ 0.28 GtC/yr (mean slope of ~~0.05~~ 0.07 GtC/yr per decade). The nCO_2 uptake is stronger than the ~~1970-2021~~ 1980-2021 mean before the mid-1990s and weaker after that ~~.~~ (Fig. 2c). On top of the long-term trend, the nCO_2 flux displays a large (~0.15 GtC/yr) decadal-scale variability. nCO_2 fluxes are strongly correlated with the SAM index calculated from the JRA-55do dataset (R=0.62 for annual mean data and R=~~0.82~~ 0.84 with a 5-year smoothing, ~~Figs. ??band S3~~Fig. 2b), with periods of weak nCO_2 uptake associated with positive phases of the SAM. ~~While this is compared to the SAM index calculated from the JRA-55do dataset (Stewart et al., 2020), similar correlations are found with the observed SAM index (Marshall, 2003).~~ This SAM link is largely related to changes in the strength of the zonal SO wind stress (Fig. ~~S3~~S5d, R=~~0.6~~ 0.62 for yearly data, ~~0.8~~ 0.92 with 5-year smoothing), even though a poleward displacement of the maximum wind stress also reduces the nCO_2 uptake (Fig. ~~S3~~S5g, R=~~-0.46). The~~ -0.4).

Since the SAM index displays a trend towards the positive phase between 1980 and 2021, the correlation mentioned above includes both interannual variability as well as decadal-scale changes. To also assess whether changes in the SAM significantly

impact nCO_2 fluxes on an interannual timescale, we look into the detrended SAM and nCO_2 flux time-series (Fig. 3b and c). The correlation between the detrended SAM index and detrended nCO_2 ~~outgassing occurs in the SO upwelling area (south of 55~~flux is significant ($p \leq 0.05$) and equals 0.46. We however note that if the detrended SAM index is averaged over two years (mean of the current and previous year), then the correlation equals 0.8 (Fig. S5a), indicating that the atmospheric forcing during the previous year also impacts surface natural pCO_2.

To assess the impact of high-resolution, and thus the lack of parametrised eddies, on the simulated CO_2 fluxes, the results of the 1° ~~S), but also up to 50°S due to the northward advection DIC-rich waters~~ version of ACCESS-OM2 are also included (Fig. ~~1c, e).~~ 2c, blue). If zonally-averaged, they closely track the results of ACCESS-OM2-01, displaying a similar trend and interannual variability in SO nCO_2 fluxes.

The simulated aCO_2 uptake increases by ~~0.8~~ 0.56 GtC/yr over the period ~~1970-2021~~ 1980-2021 (Fig. ~~??d~~2d, grey and orange) noting that the CO_{2atm} ~~growth rate~~, which is a forcing of the model, also increases ~~by 2 ppm/yr~~ during that time (Fig. ~~??~~2a). To better highlight variability in the aCO_2 flux, we detrend it and plot the anomaly with respect to the ~~1970-2021~~ 1980-2021 mean (Fig. ~~??e~~3d). The aCO_2 uptake also features decadal-scale variability, but with an amplitude that is about 30% lower than for nCO_2. A weak but significant ($p \leq 0.05$) relationship between aCO_2 uptake and the ~~SAM~~ detrended SAM index is simulated (R=~~-0.29~~0.42, Fig. ~~S3). This weak association is mostly due to the impact of stronger wind stress~~ S5b). Increased aCO_2 uptake occurs when the westerlies strengthen (R=~~0.24~~0.42, Fig. ~~S3). The increase in~~ S5e). While the 1° model displays a slightly larger aCO_2 uptake~~occurs everywhere south of 35°S, but particularly south of 50°S~~ , the trends are similar between 1980 and 2018 (Fig. ~~S2d) .~~ 2d, blue) and the detrended fluxes track each other very closely (Fig. 3d).

The combined effect of reduced nCO_2 uptake ~~,~~ and increased aCO_2 uptake (mostly due to the increase in CO_{2atm}) lead to a ~~0.55~~ 0.36 GtC/yr increase in tCO_2 uptake between ~~1970~~ 1980 and 2021 (Fig. ~~??f~~2e). The SO tCO_2 uptake ~~also features decadal-scale variability, with a stagnation of tCO_2 uptake between 1982 and 2000, a reinvigoration in the early 2000s and only~~ ~in the 0.1° and 1° simulations track each other fairly closely, even though the trend is larger in the 1° (-0.015 GtC/yr~~increase since 2010.~~ ^{2}) than in the 0.1° (-0.013 GtC/yr^2) (Fig. 2e, blue compared to grey). The simulated tCO_2 fluxes can be compared to the observational estimates derived from the SOM-FFN ~~and~~ based on the ~~Surface Ocean CO2 Atlas Database (SOCAT) and Southern Ocean Carbon and Climate Observations and Modeling (SOCCOM)~~ SOCAT and SOCCOM biogeochemistry floats from 1982 to 2017 ~~(Landschützer et al., 2019; Bushinsky et al., 2019) (Fig. ??h~~(red) (Landschützer et al., 2019; Bushinsky et al., 2019), and based on SOCAT only from 1982 to 2021 (magenta) (Landschützer et al., 2020) (Fig. 2g). The simulated tCO_2 flux and observational estimates of tCO_2 flux are well correlated (R=0.55 ~~) and both display minimum~~ for SOCAT+SOCCOM compared to ACCESS-OM2-01 and R=0.79 for SOCAT only compared to ACCESS-OM2-01).

In the 0.1° experiment, the simulated tCO_2 uptake increases by only 0.003 GtC/yr^2 between 1980 and 1998 (Fig. 2e), in agreement with both observational estimates (Fig. 2f). While the simulated tCO_2 uptake ~~in 2000-2001,~~ decreases between 1998 and ~~maximum in the early 1990s and early 2010s. While the simulated amplitude of the variations is about half of the observed one, it is~~ 2001 as in the observations, the magnitude of this simulated change is smaller than in the observational estimates. Similarly, while both simulation and observational estimates display an increase in tCO_2 uptake in the early 2000s, the reinvigoration only lasts until 2003 in the simulation, while it lasts until 2010 in both observational datasets. Finally,

similar to the SOCAT only product, the simulation suggests a stagnation of the tCO_2 uptake between 2011 and 2018, while the SOCAT+SOCCOM product suggests a decrease in tCO_2 uptake. While the simulated tCO_2 changes are within the uncertainty range of the observational ~~estimate~~ estimates (~~±0.25~~ 0.15 GtC/yr) (Bushinsky et al., 2019) ~~.~~ for most of the simulated period, the simulated variations are lower and outside of the uncertainty range between 1998 and 2005.

Since changes in tCO_2 flux are also impacted by the CO_{2atm} increase, we detrend the SO tCO_2 flux and plot the anomaly with respect to the detrended ~~1970-2021~~ 1980-2021 mean to properly assess the decadal-scale variability~~(Fig. ??g).~~. The detrended tCO_2 ~~flux thus presents~~ fluxes (Fig. 3e) present variations similar to the detrended nCO_2 fluxes (Fig. 3c), with reduced total uptake during positive phases of the SAM ~~.~~ (Fig. 3b). The nCO_2 flux variability dominates the changes in tCO_2 uptake with a strengthening of the winds and a poleward shift both reducing the tCO_2 uptake (Figs. ~~??c,g and S3).~~ 3c,e and S5f,i). The detrended fluxes in the 0.1° and 1° simulations track each other very closely (Fig. 3e).

The correlation between detrended simulated and observationally estimated tCO_2 fluxes are 0.35 for SOCAT+SOCCOM (Bushinsky et al., 2019) and 0.37 for SOCAT only Landschützer et al. (2020). The two main disagreements are in the mid 1990s and the late 2000s/early 2010s, when the model simulates relatively low tCO_2 uptake (Fig. 3e) while the observational estimates suggest high tCO_2 uptake (Fig. 3f). During these two periods the detrended nCO_2 fluxes are small, whereas the detrended aCO_2 fluxes are positive. These periods of low tCO_2 uptake in the model are thus due to reduced aCO_2 uptake, probably resulting from the atmospheric CO_2 forcing.

3.3 Processes leading to changes in natural CO_2 fluxes

3.3.1 Multi-decadal trend

To better understand the ~~changes in~~ processes driving the multi-decadal increase in SO nCO_2 ~~flux we calculate the changes in surface~~ outgassing, we look into the surface water natural pCO_2 ~~arising from thermal and non-thermal (sum of nDIC, alkalinity and salinity) contributions in the different sectors of the Southern Ocean (~~trend and the contributions to this trend of changes in nDIC, ALK, surface temperature (SST) and salinity (SSS, Fig. 4) ~~. As the outgassing of nCO_2 occurs south of the SAF, we focus our analysis on that region. The~~ in the ACCESS-OM2-01.

The largest positive natural pCO_2 ~~increase south of 50~~trend is simulated south of the PF and particularly south of 60°S~~since the 1990s is due to non-thermal contributions. Given that the surface salinity changes are negligible, this increase is thus due to higher surface nDIC ~~, in the area of high upward Ekman pumping (Fig. 1e). The natural pCO_2 trends are particularly large in the Atlantic and Indian sectors. This is due to an increase in surface nDIC (Fig. 4b), partly compensated by an increase in ~~surface alkalinity. Changes in SST oppose the non-thermal pCO_2 changes, with a decrease in SST during positive phases of the SAM. The non-thermal pCO_2 evolution, which closely follows the nCO_2 fluxes~~ ALK (Fig. ~~S4), differs in each sector. In particular,~~ 4c). We also note an area displaying a negative natural pCO_2 ~~variations in the Pacific sector are significant throughout the period but do not display a clear trend~~trend, off the Ross Sea and extending eastward. This is due to a decrease in nDIC, partly compensated by a decrease in ALK. On the other hand, the ~~Indian and Atlantic pCO_2 variations are negligible until the mid to late 1990s but match the Pacific contribution in 2015/2016. These changes in~~ changes in SST and SSS (Fig. 4d,e) are not

contributing significantly to the multi-decadal changes in surface natural pCO_2~~, and thus nCO_2 fluxes impact the tCO_2 fluxes, with lower tCO_2 uptake in the Pacific basin in the late 1990s compared to the other basins, whereas the Pacific tCO_2 uptake is higher in the Pacific than in the other basins in the 2010s~~ .

Taking also into account that changes in detritus flux are concentrated north of 50°S (Fig. S3k), these results suggest that changes in oceanic circulation, and particularly the upwelling strength (Fig. ~~S4) , in agreement with observations (Keppler and Landschützer~~

S3j) and subsequent northward Ekman transport (Fig. S3i), are responsible for the positive nCO_2 outgassing trend (Figs. 2c and S3l). The non-thermal natural pCO_2 changes are indeed significantly correlated with changes in the strength of the westerlies in each sector of the Southern Ocean (Fig. 4S6a,d). The inter-basin differences in SH westerlies latitudinal trends probably contributed to the relatively larger increase in surface natural pCO_2 in the Atlantic and Indian sectors compared to the Pacific sector ~~.~~(Fig. S6e). Indeed, in the JRA55-do dataset there is a $\sim$1.5° and $\sim$1° poleward shift in the Atlantic and Indian sectors, respectively starting in the late 1990s, while there are no significant latitudinal changes in the Pacific sector (Fig. ~~S5~~S6e). This is broadly consistent with observations, which suggest a $\sim$1° poleward shift in the Atlantic and Indian sector and a $\sim$1° equatorward shift in the Pacific sector since the 1980s (Waugh et al., 2020).

~~Overall, an increase in surface~~ The processes leading to the positive natural pCO_2 ~~is simulated as a response~~ trend can be further assessed by analysing the changes in SO nDIC between 1980 and 2021 (Fig. 5). An increase in nDIC is simulated within the upwelling branches of the North Atlantic Deep Water, Indian Deep Water and Pacific Deep Water (Fig. 5a-c), while the nDIC concentration is reduced below 3000m depth, particularly in the Atlantic and Indian sectors as well as within the SAMW. The nDIC increases within the upwelling branches are mostly due to an increase in ~~surface nDIC, with a small contribution from~~ remineralized DIC (Fig. 5d-f). It is unlikely that the detritus flux increase centered at 42°S (Fig. S3k) is responsible for these positive remineralized DIC anomalies, instead they most likely indicate a higher proportion of older/deeper waters, consistent with enhanced SO upwelling.

The negative nDIC anomalies at depth are concentrated in the Antarctic Bottom Water (AABW) formation regions (Weddell Sea, Ross Sea and Adelie coast), and in the subsequent transport regions westward around Antarctica (Morrison et al., 2020; Solodoch et al. The negative nDIC anomalies at depth and within the SAMW are due to reduced remineralized DIC content, most likely implying higher transport rates of SAMW and AABW.

A reduced vertical nDIC gradient is simulated in all basins south of the SAF, due to higher nDIC in the top $\sim$1000m depth and reduced nDIC at depth. This pattern is consistent with enhanced SO upwelling resulting from a strengthening and poleward shift of the SH westerlies since 1980.

We next look at the evolution of nDIC in the subsurface of the SO between 1980 and 2021, and assess its link to the surface variability (Fig. 6). The nDIC concentration at 1000m depth gradually increases at all latitudes during that time period, but with a steepest increase between 45°S and 60°S (Fig. 6b), which corresponds to the upwelling branch of the Indian Deep Water, Pacific Deep Water and North Atlantic Deep Water. At 400m depth, nDIC also increases south of the SAF due to the enhanced upwelling of nDIC-rich deep waters (Fig. 6a). On the other hand, nDIC at 400m depth decreases north of the SAF within SAMW. This contrasting behavior north and south of the SAF could be linked to the poleward shift of the SH westerlies.

At both 400m and 1000m depth, decadal-scale DIC variations are visible (Fig. 6). The fast response of subsurface DIC to the surface forcing is consistent with nDIC changes being due to Ekman pumping and associated isopycnal displacement, which respond quickly to surface forcing (Waugh and Haine, 2020).

3.3.2 Impact of the SAM on SO CO_2 fluxes

Overall, an increase in ~~SST since the late 2010s.~~ natural CO_2 outgassing is simulated in SO (Fig. 2c) as a response to an increase in surface nDIC. Superimposed on this trend are increases in ~~pCO~~nCO_2 ~~driven by higher nDIC~~ outgassing during positive phases of the SAM ~~.~~ (Figs. 2b,c and 3b,c). To better highlight the quantitative impact of positive phases of the SAM, we perform a composite of the years in which the annual mean SAM index as calculated from the JRA55-do dataset was greater than ~~0.83~~ 0.33 (i.e. 1998, 1999, 2010, 2015 and 2021) and compare this to a composite of negative SAM years (SAM index$\leq$-0.33: 1980, 1991, 1992, 2002).

During these strong positive phases of the SAM, a significant increase ($\geq$1 mol/m^2/yr) in nCO_2 outgassing is simulated south of the PF (Fig. 7a). Some enhanced nCO_2 outgassing is also simulated between the SAF and PF in the Indian and southwest Pacific sector as well as north of the SAF in the Pacific sector. This nCO_2 outgassing mostly results from an increase in surface nDIC concentration (Fig. 7b, 9b).

The stronger and poleward shifted westerlies during positive phases of the SAM enhance the Ekman-driven vertical DIC advection south of the PF (Figs. 7g and 8b). The associated deepening of the mixed layer also drives an increase in vertical DIC diffusion at the base of the mixed layer (Figs. 7e,f and 8c). South of the PF, the Ekman-driven vertical DIC advection and vertical diffusion at the base of the mixed layer contribute equally to the DIC increase (2.8 GtC/yr, Fig. 8b,c). The eddy-driven vertical DIC advection (taken as the difference between the vertical DIC advection and the Ekman-driven vertical DIC advection) further contributes to the higher surface DIC south of 60°S (+0.7 GtC/yr, not shown). However, north of the PF, the Ekman-driven vertical DIC advection decreases surface DIC, while vertical diffusion at the base of the mixed layer leads to a DIC increase in the mixed layer. In this simulation, changes in biological export of carbon are two ~~order~~ orders of magnitude smaller than the Ekman-driven and vertical diffusion contributions and therefore do not affect significantly changes in nCO_2 fluxes (Fig. 8d).

Due to the long-term shift towards positive phases of the SAM, the composite of positive SAM is shifted towards more recent years than the composite of negative phases. If we correct for this (i.e. assuming that the aCO_2 uptake follows a linear trend), then an anomalous aCO_2 uptake is simulated south of the PF (Fig. 7c), in regions where a stronger nCO_2 outgassing is simulated (Fig. 7a). The amplitude of the aCO_2 anomalies are however only equivalent to $\sim$25% of the nCO_2 anomalies (Figs. 7~~8~~a,c and 8e,f black line). As a result, reduced tCO_2 uptake is simulated south of the PF during positive phases of the SAM (Fig. ~~S6~~S7b). If a similar correction is applied to compensate for the difference in mean year between the positive and negative SAM composites, then an anomalous tCO_2 outgassing is simulated almost everywhere in the SO (Figs. 7d and 8g, black line).

It is interesting to note that south of the PF, the ~~structure of the mean~~ regions of maximum nCO_2 outgassing and aCO_2 ~~fluxes~~ uptake averaged over the period ~~1981-2021~~ 1982-2021 (Fig. 1c,d) are similar to the maximum nCO_2 outgassing and aCO_2 uptake anomalies obtained for positive phases of the SAM (Fig. 7a,c), indicating that the positive phases of the SAM simply

accentuate the mean SO features (i.e. nCO_2 outgassing gets stronger in outgassing regions). ~~This is however not the case north of the SAF in the Pacific sector, where the nCO_2 uptake is reduced during positive phases of the SAM.~~

Some of the main areas of nCO_2 outgassing and aCO_2 uptake correspond to major topographic features of the SO: namely, the eastern part of the Southeast Indian Ridge, ~~the~~ Drake Passage and the Southwest Indian Ridge (Fig. ~~1e~~1c,d,e). On the contrary, the cyclonic circulation in the relatively deep basin of the eastern part of the Ross Sea and Amundsen-Bellinghausen Sea is associated with nCO_2 uptake. This could be due to enhanced eddy mixing over topography linked to the merging of multiple jets (Lu and Speer, 2010), and warrants further study.

3.4 ~~Changes in oceanic DIC~~

~~We now look into the changes in oceanic natural, anthropogenic and total DIC concentration between 1980 and 2021 in the different sectors of the Southern Ocean. As discussed above, the outgassing of natural carbon in the SO increases with wind stress as the upwelling of DIC-rich waters and vertical diffusion at the base of the mixed layer are enhanced. An increase in nDIC is simulated within the upper Circumpolar Deep Water (CDW), particularly in the Pacific sector and somewhat in the Indian sector (Fig. 5d-f). This increase is linked to higher nDIC within the Indian and Pacific deep waters (IDW and PDW, respectively). Higher nDIC is also simulated within the upwelling branch of the North Atlantic Deep Water in the Atlantic sector. These nDIC increases are associated with negative dissolved oxygen (O_2) anomalies (Fig. 5a-e) and are due to an increase in remineralized DIC (Fig. S7), thus indicating a higher proportion of older/deeper waters. On the other hand, a decrease in nDIC is simulated within the SAMW, the lower CDW, and within AABW. The negative nDIC anomalies at depth are mostly visible in the Atlantic and Indian sectors as the anomalies are concentrated in the AABW formation regions (Weddell Sea, Ross Sea and Adelie coast), and their subsequent transport westward around Antarctica (Morrison et al., 2020; Solodoch et al., 2022). The negative nDIC anomalies are due to reduced remineralized DIC content and are associated with positive O_2 anomalies. This implies either reduced nutrient utilisation in the Southern Ocean and/or higher transport rates of SAMW and AABW.~~

~~The strengthening and poleward shift of the SH westerlies since 1980 also impacts the nDIC distribution within the SO with a reduced vertical gradient south of the SAF, linked to a reduction in regenerated carbon at depth. This weaker biological pump efficiency in 2017-2021 compared to 1980-1982 could result from the lower residence time in the SO, arising from the higher SO upwelling rate and potentially higher mixing at depth due to the poleward intensified westerlies, and associated changes in windstress curl (Fig. S2).~~

~~We next look at the evolution of nDIC in the subsurface of the SO between 1980 and 2021, and assess its link to the surface variability (Fig. 6). The nDIC concentration at 1000m depth gradually increases at all latitudes during that time period, but with a steepest increase between 45°S and 60°S, which corresponds to the upwelling branch of the IPW, PDW and NADW. At 400m depth, nDIC also increases south of the SAF due to the enhanced upwelling of nDIC-rich deep waters. On the other hand, nDIC at 400m depth decreases north of the SAF within SAMW. This contrasting behavior north and south of the SAF could be linked to the poleward shift of the SH westerlies. At both 400m and 1000m depth, decadal-scale DIC variations are visible.~~

The fast response of subsurface DIC to the surface forcing is consistent with nDIC changes being due to Ekman pumping and associated isopycnal displacement, which respond quickly to surface forcing (Waugh and Haine, 2020).

In the simulation presented here, the Southern Ocean absorbs 27 Gt of anthropogenic carbon between 1970 and 2021. In the SO, the highest increase is within AAIW and SAMW, in agreement with observations (Gruber et al., 2019a) (Fig. S8). A minor part of anthropogenic DIC (aDIC) is also entrained within AABW. As expected due to relative water-mass ventilation rates, the smallest increase in aDIC is simulated within the upper CDW of the Pacific basin, while relatively large ($\geq$5 mmol/m^3) increases in aDIC can be seen close to the Antarctic shelf in the Indian sector between 1980 and 2021. This could be linked to the deepening of the mixed layer depth off the Adelie coast in the model runs.

If we assume a linear increase in oceanic aDIC based on the simulated accumulation in the 1970s (Gruber et al., 2019a), then the anomalous aDIC concentration is high ($\geq$ 5 mmol/m^3) within AAIW and SAMW as well as within the upper 500 m on the Antarctic shelf (Fig. 5g-i), indicating enhanced entrainment of aDIC within these water-masses and potentially AABW. Small negative aDIC anomalies are however simulated within the upwelling branch of IDW, and to a lesser extent NADW and PDW. These correspond to regions with positive nDIC and remineralized DIC anomalies as well as negative O_2 anomalies, thus confirming the increased proportion of older, DIC-rich deep waters.

As a result the corrected total DIC (from which the linear aDIC increase has been removed) increases within SAMW, AAIW and the upper CDW by 19 mmol/m^3, 11 mmol/m^3 and 3 mmol/m^3, respectively, while there are little changes below 2000 m depth, or even small negative anomalies in the deep Atlantic and Indian Oceans (Fig. 5j-l). This indicates a reduction in the vertical tDIC gradient in the Southern Ocean.

4 Discussion and conclusions

We have used an eddy-rich global ocean, sea-ice, carbon cycle model to assess changes in SO total, natural and anthropogenic CO_2 fluxes over the last 50 years. The multi-decadal strengthening and poleward shift of the SH westerlies, associated with a shift towards positive phases of the SAM during that period, drives a decrease in nCO_2 uptake with a trend of -0.007 GtC/yr^2. On the other hand, the increase in CO_{2atm} growth rate leads to a higher aCO_2 uptake with a trend of 0.014 PgCGtC/yr^2. The results presented here suggest that the A strengthening and poleward shift of the SH westerlies only had a small impact on enhance the aCO_2 uptake but the magnitude of this change is only 30% of the associated enhanced nCO_2 outgassing. As a result, while the tCO_2 uptake increases between 1980 and 2021 with a trend of 0.007 PgCGtC/yr^2, it would have likely increased twice as fast without a strengthening and poleward shift of the SH westerlies. These CO_2 flux trends simulated with a high-resolution eddy-rich model are similar to those obtained by a similar simulation performed with ACCESS-OM2 at 1° resolution (Fig. 2), even though the nCO_2 trend is slightly smaller (-0.005 GtC/yr^2) and the tCO_2 trend larger (0.009 GtC/yr^2) in the 1° than the 0.1° experiment. These results are also consistent with those of Lovenduski et al. (2008), who simulated an increase in nCO_2 outgassing between 1979 and 2004 with a trend of 0.004 PgCGtC/yr^2, an increase in aCO_2 uptake with a trend of 0.011 PgCGtC/yr^2 and thus an increase in tCO_2 uptake of 0.007 PgCGtC/yr^2 using a coarse resolution ocean model.

The multi-decadal, large-scale oceanic carbon cycle response to a strengthening and poleward shift of the SH westerlies is thus robust from eddy-rich to coarse resolution models.

In addition, the total air-sea CO_2 fluxes exhibit large ($\sim$0.1 GtC/yr) decadal-scale variability thus supporting previous inferences of decadal scale changes in SO CO_2 fluxes (Li and Ilyina, 2018; Lovenduski et al., 2008; Landschützer et al., 2015; Gruber et al., 2019b). The simulated variability is not as large as that derived from observational estimates ($\sim$0.25 GtC/yr) (Landschützer et al., 2016; Bushinsky et al., 2019; Keppler and Landschützer, 2019), but is within the uncertainty band ($\pm$0.15 GtC/yr) (Gruber et al., 2019b; Bushinsky et al., 2019). Such a mismatch between simulated SO tCO_2 variations and observations is prevalent in hindcast simulations (Gruber et al., 2019b) ~~. It should be noted that it has been suggested that~~ and could be due to an overestimation of the observed SO CO_2 flux variability ~~could be overestimated (Gloege et al., 2021). In addition, the~~ (Gloege et al., 2021). The underestimation of the ~~simulated~~ changes in tCO_2 uptake in the ~~late 2000s/early 2010s could~~ simulation could also be due a ~~mis-representation~~ misrepresentation of Southern Ocean stratification. It has indeed been suggested that the overturning rate of the lower cell ~~was weaker during that time period~~ weakened in the 2000s (DeVries et al., 2017) due to enhanced stratification in the Southern Ocean (de Lavergne et al., 2014), linked to enhanced Antarctic basal melt rates (Adusumilli et al., 2020). Enhanced stratification in the Southern Ocean would weaken the aCO_2 uptake (Bourgeois et al., 2022), but would reduce the nCO_2 outgassing (Menviel et al., 2015), thus potentially enhancing tCO_2 uptake.

To first order, the simulated ~~decadal scale~~ decadal-scale changes in tCO_2 fluxes are due to changes in nCO_2 fluxes primarily arising from changes in the magnitude of the SH westerlies, but also due to variations in the latitudinal position of the SH winds. While we find a strong link between regional wind changes and nCO_2/tCO_2 fluxes, we find that minima in tCO_2 uptake arise from a strengthening and/or poleward shift of the SH westerlies, and thus positive phases of the SAM. This is in contrast to the conclusion of Keppler and Landschützer (2019) that the SAM had a net zero effect on SO tCO_2 uptake. Both our study and the one of Keppler and Landschützer (2019) highlighted enhanced tCO_2 outgassing south of 50°S during positive phases of the SAM as well as zonal asymmetries with enhanced tCO_2 uptake in the Pacific sector of the SO. While Keppler and Landschützer (2019) suggest this is linked to the zonal wave number 3 pattern, we attribute these asymmetries to the bathymetry and different poleward trends of the westerlies in the different sectors of the SO.

A stagnation of SO tCO_2 uptake between 1980 and 2000 is simulated. This time period corresponds to the largest rate of increase and shift in westerly wind stress~~increase, but also a poleward shift of the westerlies~~. The timing and magnitude of this stagnation in tCO_2 uptake in the SO is in agreement with observational estimates (Lovenduski et al., 2008; Landschützer et al., 2015; Gruber et al., 2019b; Keppler and Landschützer, 2019). While the impact of the SAM on SO CO_2 fluxes is clear in our simulation, the early 1990s also feature the lowest atmospheric CO_2 growth rate of the period studied here (McKinley et al., 2020). The simulated SO aCO_2 uptake in the early 1990s is thus the lowest of the period, noting that positive phases of the SAM are usually associated with slightly enhanced aCO_2 uptake. Our results thus also support the conclusion that the slowdown of the SO tCO_2 uptake in the early 1990s was due to a low atmospheric CO_2 growth rate (McKinley et al., 2020) and not a positive phase of the SAM (LeQuéré et al., 2007; Lovenduski et al., 2008; Matear and Lenton, 2008). In agreement with observations, a re-invigoration of tCO_2 uptake is simulated in the early 2000s (Keppler and Landschützer, 2019), mostly

due to a pause in the positive SAM trend. Since the mid 2000s, the tCO_2 uptake has increased slowly, but we find that the reversal in tCO_2 uptake that had been highlighted in the mid 2010s (Keppler and Landschützer, 2019) was short-lived and due to the strong positive 2015 SAM.

The enhanced nCO_2 outgassing during positive phases of the SAM is due to higher surface nDIC concentration south of the PF, partly compensated by lower SST. This increase in surface nDIC results from enhanced vertical nDIC advection, mostly Ekman driven, as well as enhanced vertical nDIC diffusion at the base of the mixed layer. This significant role of vertical diffusion is in agreement with a previous study performed with an eddy-permitting model (Dufour et al., 2013), even if contrarily to that study we find an equal weight of vertical advection and Ekman pumping south of the PF. The dominance of Ekman driven vertical nDIC advection also explains the similar results obtained in the high and coarse resolution versions of the ACCESS-OM2. As in previous studies, we ~~find that biological processes do not significantly impact air-sea~~ thus find that changes in oceanic circulation are the primary driver of changes in SO CO_2 fluxes on decadal-time scales ~~, and that the changes in surface nDIC arise from changes in oceanic circulation (Dufour et al., 2013)~~(Dufour et al., 2013; Resplandy et al., 2015; Nevison et al., 2

Previous studies have suggested that wind-driven changes in oceanic circulation in the Southern Ocean are partially compensated by the eddy-driven transport (Morrison and Hogg, 2013). Similarly, Dufour et al. (2013) suggested that 1/3 of the Ekman-driven DIC transport arising from positive phases of the SAM was compensated by eddy transport. Here, despite a 20% increase in wind stress, only a small ACC increase (134 to 138 Sv) is simulated thus supporting the eddy saturation theory. Yet, we find that changes in the position and strength of the SH westerlies lead to an outgassing of nCO_2 on a yearly as well as multi-decadal timescale, with an amplitude similar to that found in ~~previous studies performed with coarser resolutionmodels (Dufour et al., 2013; Lovenduski et al., 2007)~~a similar model (ACCESS-OM2) with a 1° resolution. This is an important result as it was suggested that mesoscale eddies would compensate for the wind-driven circulation in the Southern Ocean, thus mitigating the carbon cycle response to changes in the strength and position of the westerlies. Here we show that even in an eddy-rich model, a strengthening and/or a poleward shift of the westerlies leads to enhanced CO_2 outgassing. This further suggests that ocean models with a ~1° resolution correctly capture the large-scale carbon cycle response to changes in the SH westerlies. It should however be noted that in the 1° ocean model used here, the GM coefficient varies in space and time (Kiss et al., 2020). While both the 0.1° and 1° resolution simulations display broadly similar mean CO_2 fluxes (Figs. 1 and S4) and CO_2 fluxes response to positive phase of the SAM (Figs. 7 and S8), higher nCO_2 outgassing is simulated south of the PF in the 0.1° than 1° resolution. This could be due to larger upwelling downstream of topographic features in the eddy-rich version of the model.

If SH westerly winds continue to strengthen, as projected under RCP8.5/SSP5-85 scenarios (Grose et al., 2020; Goyal et al., 2021), our experiments suggest that the increase in aCO_2 uptake would be partly compensated by nCO_2 outgassing, thus ~~only leading to~~ leading to only a small increase in tCO_2 uptake. Future changes in SO carbon uptake will thus likely result from a fine balance between natural carbon release and anthropogenic carbon uptake, which will itself depend on changes in SH westerlies, SO stratification and temperature as well as the rate of anthropogenic carbon emissions.

Acknowledgements. This project was supported by the Australian Research Council (ARC), including grants FT180100606, FT190100413, and SR200100008 AEK was supported by ARC grants LP160100073 and LP200100406, and the Australian Government's Australian Antarctic Science Program grant 4541.

The authors thank the Consortium for Ocean-Sea Ice Modelling in Australia (COSIMA; http://www.cosima.org.au) for making the ACCESS-OM2 suite of models available at https://github.com/COSIMA/access-om2. Model runs were undertaken with the assistance of resources from the National Computational Infrastructure (NCI), which is supported by the Australian Government. The authors thank Kial Stewart for sharing the code to calculate the SAM index from the JRA-55do dataset.

Data availability The modelling outputs presented here have been deposited on UNSWorks (https://unsw-primo.hosted.exlibrisgroup.com/primo-explore/search?vid=UNSWORKS). A doi will be generated upon acceptance of the manuscript.

References

Adusumilli, S., Fricker, H., Medley, B., Padman, L., and Siegfried, M.: Interannual variations in meltwater input to the Southern Ocean from Antarctic ice shelves, Nature Geosciences, 13, 616–620, https://doi.org/10.1038/s41561-020-0616-z, 2020.

Arblaster, J. M. and Meehl, G. A.: Contributions of External Forcings to Southern Annular Mode Trends, Journal of Climate, 19, 2896–2905, https://doi.org/10.1175/JCLI3774.1, 2006.

Bakker, D. C. E., Pfeil, B., Landa, C. S., Metzl, N., O'Brien, K. M., Olsen, A., Smith, K., Cosca, C., Harasawa, S., Jones, S. D., Nakaoka, S., Nojiri, Y., Schuster, U., Steinhoff, T., Sweeney, C., Takahashi, T., Tilbrook, B., Wada, C., Wanninkhof, R., Alin, S. R., Balestrini, C. F., Barbero, L., Bates, N. R., Bianchi, A. A., Bonou, F., Boutin, J., Bozec, Y., Burger, E. F., Cai, W.-J., Castle, R. D., Chen, L., Chierici, M., Currie, K., Evans, W., Featherstone, C., Feely, R. A., Fransson, A., Goyet, C., Greenwood, N., Gregor, L., Hankin, S., Hardman-Mountford, N. J., Harlay, J., Hauck, J., Hoppema, M., Humphreys, M. P., Hunt, C. W., Huss, B., Ibánhez, J. S. P., Johannessen, T., Keeling, R., Kitidis, V., Körtzinger, A., Kozyr, A., Krasakopoulou, E., Kuwata, A., Landschützer, P., Lauvset, S. K., Lefèvre, N., Lo Monaco, C., Manke, A., Mathis, J. T., Merlivat, L., Millero, F. J., Monteiro, P. M. S., Munro, D. R., Murata, A., Newberger, T., Omar, A. M., Ono, T., Paterson, K., Pearce, D., Pierrot, D., Robbins, L. L., Saito, S., Salisbury, J., Schlitzer, R., Schneider, B., Schweitzer, R., Sieger, R., Skjelvan, I., Sullivan, K. F., Sutherland, S. C., Sutton, A. J., Tadokoro, K., Telszewski, M., Tuma, M., van Heuven, S. M. A. C., Vandemark, D., Ward, B., Watson, A. J., and Xu, S.: A multi-decade record of high-quality fCO_2 data in version 3 of the Surface Ocean CO_2 Atlas (SOCAT), Earth System Science Data, 8, 383–413, https://doi.org/10.5194/essd-8-383-2016, 2016.

Banerjee, A., Fyfe, J., Polvani, L., Waugh, D., and Chang, K.-L.: A pause in Southern Hemisphere circulation trends due to the Montreal Protocol, Nature, 579, 544–548, https://doi.org/10.1038/s41586-020-2120-4, 2020.

Bourgeois, T., Goris, N., Schwinger, J., and Tjiputra, J.: Stratification constrains future heat and carbon uptake in the Southern Ocean between 30°S and 55°S, Nat. Commun, 13, doi:10.1038/s41 467–022–27 979–5, 2022.

Broecker, W., Takahashi, T., Simpson, H., and Peng, T.-H.: Fate of fossil fuel carbon dioxide and the global carbon budget, Science, 206, 409–418, https://doi.org/10.1126/science.206.4417.409, 1979.

Bushinsky, S. M., Landschützer, P., Rödenbeck, C., Gray, A. R., Baker, D., Mazloff, M. R., Resplandy, L., Johnson, K. S., and Sarmiento, J. L.: Reassessing Southern Ocean Air-Sea CO2 Flux Estimates With the Addition of Biogeochemical Float Observations, Global Biogeochemical Cycles, 33, 1370–1388, https://doi.org/https://doi.org/10.1029/2019GB006176, 2019.

de Lavergne, C., Palter, J., Galbraith, E., Bernardello, R., and Marinov, I.: Cessation of deep convection in the open Southern Ocean under anthropogenic climate change, Nature Climate Change, 4, 278–282, https://doi.org/10.1038/NCLIMATE2132, 2014.

DeVries, T., Holzer, M., and Primeau, F.: Recent increase in oceanic carbon uptake driven by weaker upper-ocean overturning, Nature, 542, 215–218, https://doi.org/10.1038/nature21068, 2017.

Dufour, C. O., Sommer, J. L., Zika, J., Gehlen, M., Orr, J., Mathiot, J., and Barnier, B.: Standing and Transient Eddies in the Response of the Southern Ocean Merid- ional Overturning to the Southern Annular Mode, J. Climate, 25, 6958–6974, 2012.

Dufour, C. O., Sommer, J. L., Gehlen, M., Orr, J. C., Molines, J.-M., Simeon, J., and Barnier, B.: Eddy compensation and controls of the enhanced sea-to-air CO2 flux during positive phases of the Southern Annular Mode, Global Biogeochemical Cycles, 27, 950–961, https://doi.org/10.1002/gbc.20090, 2013.

Farneti, R., Delworth, T., Rosati, A., Griffies, S., and Zeng, F.: The role of mesoscale eddies in the rectification of the Southern Ocean response to climate change, J. Phys. Oceanogr., 40, 1539–1557, 2010.

Fogt, R. L. and Marshall, G. J.: The Southern Annular Mode: Variability, trends, and climate impacts across the Southern Hemisphere, WIREs Climate Change, 11, e652, https://doi.org/10.1002/wcc.652, 2020.

Friedlingstein, P., Jones, M. W., O'Sullivan, M., Andrew, R. M., Bakker, D. C. E., Hauck, J., Le Quéré, C., Peters, G. P., Peters, W., Pongratz, J., Sitch, S., Canadell, J. G., Ciais, P., Jackson, R. B., Alin, S. R., Anthoni, P., Bates, N. R., Becker, M., Bellouin, N., Bopp, L., Chau, T. T. T., Chevallier, F., Chini, L. P., Cronin, M., Currie, K. I., Decharme, B., Djeutchouang, L. M., Dou, X., Evans, W., Feely, R. A., Feng, L., Gasser, T., Gilfillan, D., Gkritzalis, T., Grassi, G., Gregor, L., Gruber, N., Gürses, O., Harris, I., Houghton, R. A., Hurtt, G. C., Iida, Y., Ilyina, T., Luijkx, I. T., Jain, A., Jones, S. D., Kato, E., Kennedy, D., Klein Goldewijk, K., Knauer, J., Korsbakken, J. I., Körtzinger, A., Landschützer, P., Lauvset, S. K., Lefèvre, N., Lienert, S., Liu, J., Marland, G., McGuire, P. C., Melton, J. R., Munro, D. R., Nabel, J. E. M. S., Nakaoka, S.-I., Niwa, Y., Ono, T., Pierrot, D., Poulter, B., Rehder, G., Resplandy, L., Robertson, E., Rödenbeck, C., Rosan, T. M., Schwinger, J., Schwingshackl, C., Séférian, R., Sutton, A. J., Sweeney, C., Tanhua, T., Tans, P. P., Tian, H., Tilbrook, B., Tubiello, F., van der Werf, G. R., Vuichard, N., Wada, C., Wanninkhof, R., Watson, A. J., Willis, D., Wiltshire, A. J., Yuan, W., Yue, C., Yue, X., Zaehle, S., and Zeng, J.: Global Carbon Budget 2021, Earth System Science Data, 14, 1917–2005, https://doi.org/10.5194/essd-14-1917-2022, 2022.

Gent, P. and McWilliams, J.: Isopycnal mixing in ocean circulation models, J. Phys. Oceanogr., 20, 150–155, 1990.

Gloege, L., McKinley, G. A., Landschützer, P., Fay, A. R., Frölicher, T. L., Fyfe, J. C., Ilyina, T., Jones, S., Lovenduski, N. S., Rodgers, K. B., Schlunegger, S., and Takano, Y.: Quantifying Errors in Observationally Based Estimates of Ocean Carbon Sink Variability, Global Biogeochemical Cycles, 35, e2020GB006 788, https://doi.org/10.1029/2020GB006788, 2021.

Goyal, R., Sen Gupta, A., Jucker, M., and England, M. H.: Historical and Projected Changes in the Southern Hemisphere Surface Westerlies, Geophysical Research Letters, 48, e2020GL090 849, https://doi.org/https://doi.org/10.1029/2020GL090849, 2021.

Gray, A. R., Johnson, K. S., Bushinsky, S. M., Riser, S. C., Russell, J. L., Talley, L. D., Wanninkhof, R., Williams, N. L., and Sarmiento, J. L.: Autonomous Biogeochemical Floats Detect Significant Carbon Dioxide Outgassing in the High-Latitude Southern Ocean, Geophysical Research Letters, 45, 9049–9057, https://doi.org/10.1029/2018GL078013, 2018.

Gregor, L., Kok, S., and Monteiro, P. M. S.: Interannual drivers of the seasonal cycle of CO_2 in the Southern Ocean, Biogeosciences, 15, 2361–2378, https://doi.org/10.5194/bg-15-2361-2018, 2018.

Griffies, S.: Elements of the Modular Ocean Model (MOM): 2012 release (GFDL Ocean Group Technical Report No. 7), Tech. rep., NOAA/-Geophysical Fluid Dynamics Laboratory, Princeton, USA, 2012.

Grose, M. R., Narsey, S., Delage, F. P., Dowdy, A. J., Bador, M., Boschat, G., Chung, C., Kajtar, J. B., Rauniyar, S., Freund, M. B., Lyu, K., Rashid, H., Zhang, X., Wales, S., Trenham, C., Holbrook, N. J., Cowan, T., Alexander, L., Arblaster, J. M., and Power, S.: Insights From CMIP6 for Australia's Future Climate, Earth's Future, 8, e2019EF001 469, https://doi.org/10.1029/2019EF001469, 2020.

Gruber, N., Clement, D., Carter, B. R., Feely, R. A., van Heuven, S., Hoppema, M., Ishii, M., Key, R. M., Kozyr, A., Lauvset, S. K., Lo Monaco, C., Mathis, J. T., Murata, A., Olsen, A., Perez, F. F., Sabine, C. L., Tanhua, T., and Wanninkhof, R.: The oceanic sink for anthropogenic CO2 from 1994 to 2007, Science, 363, 1193–1199, https://doi.org/10.1126/science.aau5153, 2019a.

Gruber, N., Landschützer, P., and Lovenduski, N.: The variable Southern Ocean carbon sink, Annual Review of Marine Science, 11, 159–186, 2019b.

Gruber, N., Bakker, D., DeVries, T., Gregor, L., Hauck, J., Landschützer, P., McKinley, G., and Müller, J.: Trends and variability in the ocean carbon sink, Nat.Rev Earth Environ., 4, 119–134, https://doi.org/https://doi.org/10.1038/s43017-022-00381-x, 2023.

Hallberg, R. and Gnanadesikan, A.: The role of eddies in determining the structure and response of the wind-driven southern hemisphere overturning : Results from the modeling eddies in the Southern Ocean (MESO) project, Journal of Physical Oceanography, 36, 2232–2252, 2006.

Hauck, J., Völker, C., Wang, T., Hoppema, M., Losch, M., and Wolf-Gladrow, D. A.: Seasonally different carbon flux changes in the Southern Ocean in response to the southern annular mode, Global Biogeochemical Cycles, 27, 1236–1245, https://doi.org/10.1002/2013GB004600, 2013.

Hayashida, H., Jin, M., Steiner, N. S., Swart, N. C., Watanabe, E., Fiedler, R., Hogg, A. M., Kiss, A. E., Matear, R. J., and Strutton, P. G.: Ice Algae Model Intercomparison Project phase 2 (IAMIP2), Geoscientific Model Development, 14, 6847–6861, https://doi.org/10.5194/gmd-14-6847-2021, 2021.

Hunke, E., Lipscomb, W., Jones, P., Turner, A., Jeffery, N., and Elliott, S.: CICE, The Los Alamos Sea Ice Model, Version 00, https://doi.org/https://www.osti.gov/biblio/1364126, 2017.

Joos, F. and Spahni, R.: Rates of change in natural and anthropogenic radiative forcing over the past 20,000 years, Proceedings of the National Academy of Sciences, 105, 1425–1430, https://doi.org/10.1073/pnas.0707386105, 2008.

Keppler, L. and Landschützer, P.: Regional Wind Variability Modulates the Southern Ocean Carbon Sink, Sci. Rep., 7384, https://doi.org/10.1038/s41598-019-43826-y, 2019.

Kidston, M., Matear, R., and Baird, M.: Parameter optimisation of a marine ecosystem model at two contrasting stations in the Sub-Antarctic Zone, Deep-Sea Research II, 58, 2301–2315, 2011.

Kiss, A. E., Hogg, A. M., Hannah, N., Boeira Dias, F., Brassington, G. B., Chamberlain, M. A., Chapman, C., Dobrohotoff, P., Domingues, C. M., Duran, E. R., England, M. H., Fiedler, R., Griffies, S. M., Heerdegen, A., Heil, P., Holmes, R. M., Klocker, A., Marsland, S. J., Morrison, A. K., Munroe, J., Nikurashin, M., Oke, P. R., Pilo, G. S., Richet, O., Savita, A., Spence, P., Stewart, K. D., Ward, M. L., Wu, F., and Zhang, X.: ACCESS-OM2 v1.0: a global ocean–sea ice model at three resolutions, Geoscientific Model Development, 13, 401–442, https://doi.org/10.5194/gmd-13-401-2020, 2020.

Landschützer, P., Gruber, N., Haumann, F. A., Rödenbeck, C., Bakker, D. C. E., van Heuven, S., Hoppema, M., Metzl, N., Sweeney, C., Takahashi, T., Tilbrook, B., and Wanninkhof, R.: The reinvigoration of the Southern Ocean carbon sink, Science, 349, 1221–1224, https://doi.org/10.1126/science.aab2620, 2015.

Landschützer, P., Gruber, N., and Bakker, D. C. E.: Decadal variations and trends of the global ocean carbon sink, Global Biogeochemical Cycles, 30, https://doi.org/10.1002/2015GB005359, 2016.

Landschützer, P., Bushinsky, S. M., and Gray, A. R.: A combined globally mapped CO_2 flux estimate based on the Surface Ocean CO2 Atlas Database (SOCAT) and Southern Ocean Carbon and Climate Observations and Modeling (SOCCOM) biogeochemistry floats from 1982 to 2017, Dataset, NOAA National Centers for Environmental Information, https://doi.org/10.25921/9hsn-xq82, 2019.

Landschützer, P., Gruber, N., and Bakker, D.: An observation-based global monthly gridded sea surface pCO2 product from 1982 onward and its monthly climatology (NCEI Accession 0160558). Version 5.5., Dataset, NOAA National Centers for Environmental Information, https://doi.org/10.7289/V5Z899N6, 2020.

Large, W. and Yeager, S.: The global climatology of an interannually varying air-sea flux data set, Clim. Dyn., 33, 341–364, 2009.

Lauderdale, J. M., Garabato, A. C. N., Oliver, K. I. C., Follows, M. J., and Williams, R. G.: Wind-driven changes in Southern Ocean residual circulation, ocean carbon reservoirs and atmospheric CO_2, Climate Dynamics, 41, 2145–2164, https://doi.org/10.1007/s00382-012-1650-3, 2013.

Lauderdale, J. M., Williams, R. G., Munday, D. R., and Marshall, D. P.: The impact of Southern Ocean residual upwelling on atmospheric CO2 on centennial and millennial timescales, Climate Dynamics, 48, 1611–1631, https://doi.org/10.1007/s00382-016-3163-y, 2017.

Law, R. M., Ziehn, T., Matear, R. J., Lenton, A., Chamberlain, M. A., Stevens, L. E., Wang, Y. P., Srbinovsky, J., Bi, D., Yan, H., and Vohralik, P. F.: The carbon cycle in the Australian Community Climate and Earth System Simulator (ACCESS-ESM1) – Part 1: Model description and pre-industrial simulation, Geoscientific Model Development, 10, 2567–2590, https://doi.org/10.5194/gmd-10-2567-2017, 2017.

Le Quéré, C., Andrew, R. M., Friedlingstein, P., Sitch, S., Pongratz, J., Manning, A. C., Korsbakken, J. I., Peters, G. P., Canadell, J. G., Jackson, R. B., Boden, T. A., Tans, P. P., Andrews, O. D., Arora, V. K., Bakker, D. C. E., Barbero, L., Becker, M., Betts, R. A., Bopp, L., Chevallier, F., Chini, L. P., Ciais, P., Cosca, C. E., Cross, J., Currie, K., Gasser, T., Harris, I., Hauck, J., Haverd, V., Houghton, R. A., Hunt, C. W., Hurtt, G., Ilyina, T., Jain, A. K., Kato, E., Kautz, M., Keeling, R. F., Klein Goldewijk, K., Körtzinger, A., Landschützer, P., Lefèvre, N., Lenton, A., Lienert, S., Lima, I., Lombardozzi, D., Metzl, N., Millero, F., Monteiro, P. M. S., Munro, D. R., Nabel, J. E. M. S., Nakaoka, S.-I., Nojiri, Y., Padin, X. A., Peregon, A., Pfeil, B., Pierrot, D., Poulter, B., Rehder, G., Reimer, J., Rödenbeck, C., Schwinger, J., Séférian, R., Skjelvan, I., Stocker, B. D., Tian, H., Tilbrook, B., Tubiello, F. N., van der Laan-Luijkx, I. T., van der Werf, G. R., van Heuven, S., Viovy, N., Vuichard, N., Walker, A. P., Watson, A. J., Wiltshire, A. J., Zaehle, S., and Zhu, D.: Global Carbon Budget 2017, Earth System Science Data, 10, 405–448, https://doi.org/10.5194/essd-10-405-2018, 2018.

Lenton, A. and Matear, R.: Role of the Southern Annular Mode (SAM) in Southern Ocean CO_2 uptake, Global Biogeochemical Cycles, 21, doi:10.1029/2006GB002 714, 2007.

LeQuéré, C., Rödenbeck, C., Buitenhuis, E., Conway, T., Langenfelds, R., Gomez, A., Labuschagne, C., Ramonet, M., Nakazawa, T., Metzl, N., Gillett, N., and Heimann, M.: Saturation of the Southern Ocean CO_2 sink due to recent climate change, Science, 316, 1735–1738, 2007.

Li, H. and Ilyina, T.: Current and Future Decadal Trends in the Oceanic Carbon Uptake Are Dominated by Internal Variability, Geophysical Research Letters, 45, 916–925, https://doi.org/10.1002/2017GL075370, 2018.

Locarnini, R., Mishonov, A., Antonov, J., Boyer, T., Garcia, H., Baranova, O. K., Zweng, M. M., Paver, C. R., Reagan, J. R., Johnson, D. R., Hamilton, M., and Seidov, D.: World Ocean Atlas 2013, vol. 1, chap. Temperature, p. 40, Ed. NOAA Atlas NESDIS 73, U.S. Government Printing Office, Washington, D.C., 2013.

Lovenduski, N., Gruber, N., Doney, S., and Lima, I.: Enhanced CO_2 outgassing in the Southern Ocean from a positive phase of the Southern Annular Mode, Global Biogeochemical Cycles, 21, doi:10.1029/2006GB002 900, 2007.

Lovenduski, N., Gruber, N., and Doney, S.: Toward a mechanistic understanding of the decadal trends in the Southern Ocean carbon sink, Global Biogeochemical Cycles, 22, doi:10.1029/2007GB003 139, 2008.

Lu, J. and Speer, K.: Topography, jets, and eddy mixing in the Southern Ocean, Journal of Marine Research, 68, 479–502, https://doi.org/10.1357/002224010794657227, 2010.

Mackallah, C., Chamberlain, M., Law, R., Dix, M., Ziehn, T., Bi, D., Bodman, R., Brown, J., Dobrohotoff, P., Druken, K., Evans, B., Harman, I., Hayashida, H., Holmes, R., Kiss, A., Lenton, A., Liu, Y., Marsland, S., Meissner, K., Menviel, L., O'Farrell, S., Rashid, H., Ridzwan, S., Savita, A., Srbinovsky, J., Sullivan, A., Trenham, C., Vohralik, P., Wang, Y.-P., Williams, G., Woodhouse, M., and Yeung, N.: ACCESS datasets for CMIP6: methodology and idealised experiments, Journal of Southern Hemisphere Earth Systems Science, 72, 93–116, https://doi.org/10.1071/ES21031, 2022.

Marshall, G.: Trends in the Southern Annular Mode from observations and reanalyses, J. Clim., 16, 4134–4143, 2003.

Matear, R. and Lenton, A.: Impact of Historical Climate Change on the Southern Ocean Carbon Cycle, Journal of Climate, 21, 5820–5834, https://doi.org/10.1175/2008JCLI2194.1, 2008.

McKinley, G. A., Fay, A. R., Eddebbar, Y. A., Gloege, L., and Lovenduski, N. S.: External Forcing Explains Recent Decadal Variability of the Ocean Carbon Sink, AGU Advances, 1, e2019AV000 149, https://doi.org/10.1029/2019AV000149, e2019AV000149 2019AV000149, 2020.

Menviel, L., Timmermann, A., Mouchet, A., and Timm, O.: Climate and marine carbon cycle response to changes in the strength of the southern hemispheric westerlies, Paleoceanography, 23, doi:10.1029/2007PA001 604, 2008.

Menviel, L., Mouchet, A., Meissner, K., Joos, F., and England, M.: Impact of oceanic circulation changes on atmospheric $\delta^{13}CO_2$, Global Biogeochemical Cycles, 29, 1944–1961, https://doi.org/10.1002/2015GB005207, 2015.

Menviel, L., Spence, P., Yu, J., Chamberlain, M., Matear, R., Meissner, K., and England, M.: Southern Hemisphere westerlies as a driver of the early deglacial atmospheric CO_2 rise, Nature Communications, 9, 2503, https://doi.org/10.1038/s41467-018-04876-4, 2018.

Mikaloff-Fletcher, S., Gruber, N., Jacobson, A., Doney, S., Dutkiewicz, S., Gerber, M., Follows, M., Joos, F., Lindsay, K., Menemenlis, D., Mouchet, A., Müller, S., and Sarmiento, J.: Inverse estimates of anthropogenic CO_2 uptake, tranport, and storage by the ocean, Global Biogeochemical Cycles, 20, GB2002, https://doi.org/10.1029/2005GB002530, 2006.

Morrison, A. and Hogg, A.: On the Relationship between Southern Ocean Overturning and ACC Transport, J. Phys. Oceanogr., 43, 140–148, https://doi.org/10.1175/JPO-D-12-057.1, 2013.

Morrison, A. K., Hogg, A. M., England, M. H., and Spence, P.: Warm Circumpolar Deep Water transport toward Antarctica driven by local dense water export in canyons, Science Advances, 6, eaav2516, https://doi.org/10.1126/sciadv.aav2516, 2020.

Munday, D. R., Johnson, H. L., and Marshall, D. P.: Eddy Saturation of Equilibrated Circumpolar Currents, Journal of Physical Oceanography, 43, 507 – 532, https://doi.org/10.1175/JPO-D-12-095.1, 2013.

Munday, D. R., Johnson, H. L., and Marshall, D. P.: Impacts and effects of mesoscale ocean eddies on ocean carbon storage and atmospheric pCO2, Global Biogeochemical Cycles, 28, 877–896, https://doi.org/10.1002/2014GB004836, 2014.

Nevison, C. D., Munro, D. R., Lovenduski, N. S., Keeling, R. F., Manizza, M., Morgan, E. J., and Rödenbeck, C.: Southern Annular Mode Influence on Wintertime Ventilation of the Southern Ocean Detected in Atmospheric O2 and CO2 Measurements, Geophysical Research Letters, 47, e2019GL085 667, https://doi.org/https://doi.org/10.1029/2019GL085667, 2020.

Oke, P., Griffin, D., Schiller, A., Matear, R., Fiedler, R., Mansbridge, J., Lenton, A., Cahill, M., Chamberlain, M., and Ridgway, K.: Evaluation of a near-global eddy-resolving ocean model, Geoscience Model Development, 6, 591–615, https://doi.org/10.5194/gmd-6-591-2013, 2013.

Olsen, A., Key, R. M., van Heuven, S., Lauvset, S. K., Velo, A., Lin, X., Schirnick, C., Kozyr, A., Tanhua, T., Hoppema, M., Jutterstrom, S., Steinfeldt, R., Jeansson, E., Ishii, M., PÃ©rez, F. F., and Suzuki., T.: The Global Ocean Data Analysis Project version 2 (GLODAPv2) - an internally consistent data product for the world ocean, Earth System Science Data, 8, 297–323, 2016.

Orr, J. C., Najjar, R. G., Aumont, O., Bopp, L., Bullister, J. L., Danabasoglu, G., Doney, S. C., Dunne, J. P., Dutay, J.-C., Graven, H., Griffies, S. M., John, J. G., Joos, F., Levin, I., Lindsay, K., Matear, R. J., McKinley, G. A., Mouchet, A., Oschlies, A., Romanou, A., Schlitzer, R., Tagliabue, A., Tanhua, T., and Yool, A.: Biogeochemical protocols and diagnostics for the CMIP6 Ocean Model Intercomparison Project (OMIP), Geoscientific Model Development, 10, 2169–2199, https://doi.org/10.5194/gmd-10-2169-2017, 2017.

Prend, C. J., Gray, A. R., Talley, L. D., Gille, S. T., Haumann, F. A., Johnson, K. S., Riser, S. C., Rosso, I., Sauvé, J., and Sarmiento, J. L.: Indo-Pacific Sector Dominates Southern Ocean Carbon Outgassing, Global Biogeochemical Cycles, 36, e2021GB007 226, https://doi.org/10.1029/2021GB007226, 2022.

Resplandy, L., Séférian, R., and Bopp, L.: Natural variability of CO2 and O2 fluxes: What can we learn from centuries-long climate models simulations?, Journal of Geophysical Research: Oceans, 120, 384–404, https://doi.org/https://doi.org/10.1002/2014JC010463, 2015.

Ritter, R., Landschützer, P., Gruber, N., Fay, A. R., Iida, Y., Jones, S., Nakaoka, S., Park, G.-H., Peylin, P., Rödenbeck, C., Rodgers, K. B., Shutler, J. D., and Zeng, J.: Observation-Based Trends of the Southern Ocean Carbon Sink, Geophysical Research Letters, 44, 12,339–12,348, https://doi.org/10.1002/2017GL074837, 2017.

Sabine, C., Feely, R., Gruber, N., Key, R., Lee, K., Bullister, J., Wanninkhof, R., Wong, C., Wallace, D., Tilbrook, B., Millero, F., Peng, T.-H., Kozyr, A., Ono, T., and Rios, A.: The oceanic sink of anthropogenic CO_2, Science, 305, 367–371, 2004.

Sarmiento, J. and Gruber, N.: Ocean Biogeochemical Dynamics, vol. 526pp, Princeton University Press, Princeton, NJ, 2006.

Sokolov, S. and Rintoul, S. R.: Circumpolar structure and distribution of the Antarctic Circumpolar Current fronts: 1. Mean circumpolar paths, Journal of Geophysical Research: Oceans, 114, https://doi.org/10.1029/2008JC005108, 2009.

Solodoch, A., Stewart, A. L., Hogg, A. M., Morrison, A. K., Kiss, A. E., Thompson, A. F., Purkey, S. G., and Cimoli, L.: How Does Antarctic Bottom Water Cross the Southern Ocean?, Geophysical Research Letters, 49, e2021GL097 211, https://doi.org/10.1029/2021GL097211, 2022.

Spence, P., Fyfe, J. C., Montenegro, A., and Weaver, A. J.: Southern Ocean response to strenghening winds in an eddy-permitting global climate model, J. Climate, 23, 5332–5343, https://doi.org/https://doi.org/10.1175/2010JCLI3098.1, 2010.

Stewart, K. D., Hogg, A., England, M. H., and Waugh, D. W.: Response of the Southern Ocean Overturning Circulation to Extreme Southern Annular Mode Conditions, Geophysical Research Letters, 47, e2020GL091 103, https://doi.org/10.1029/2020GL091103, 2020.

Tagliabue, A., Aumont, O., DeAth, R., Dunne, J. P., Dutkiewicz, S., Galbraith, E., Misumi, K., Moore, J. K., Ridgwell, A., Sherman, E., Stock, C., Vichi, M., Völker, C., and Yool, A.: How well do global ocean biogeochemistry models simulate dissolved iron distributions?, Global Biogeochemical Cycles, 30, 149–174, https://doi.org/10.1002/2015GB005289, 2016.

Takahashi, T., Olafsson, J., Goddard, J., Chipman, D., and Sutherland, S.: Seasonal-variation of CO_2 and nutrients in the high-latitude surface oceans - A comparative-study, Global Biogeochemical Cycles, 7, 843–878, 1993.

Takahashi, T., Sutherland, S., Sweeney, C., Poisson, A., Metzl, N., Tilbrook, B., Bates, N., Wanninkhof, R., Feely, R., Sabine, C., Olafsson, J., and Nojiri, Y.: Global sea-air CO_2 flux based on climatological surface ocean pCO_2 and seasonal biological and temperature effects, Deep-Sea Res. II, 49, 1601–1622, 2002.

Takahashi, T., Sutherland, S. C., Wanninkhof, R., Sweeney, C., Feely, R. A., Chipman, D. W., Hales, B., Friederich, G., Chavez, F., Sabine, C., Watson, A., Bakker, D. C., Schuster, U., Metzl, N., Yoshikawa-Inoue, H., Ishii, M., Midorikawa, T., Nojiri, Y., Körtzinger, A., Steinhoff, T., Hoppema, M., Olafsson, J., Arnarson, T. S., Tilbrook, B., Johannessen, T., Olsen, A., Bellerby, R., Wong, C., Delille, B., Bates, N., and de Baar, H. J.: Climatological mean and decadal change in surface ocean pCO2, and net sea–air CO2 flux over the global oceans, Deep Sea Research Part II: Topical Studies in Oceanography, 56, 554–577, https://doi.org/10.1016/j.dsr2.2008.12.009, 2009.

Thompson, D. and Solomon, S.: Interpretation of recent southern hemisphere climate change, Science, 296, 895–899, 2002.

Thompson, D., Solomon, S., Kushner, P., England, M., Grise, K., and Karoly, D.: Signatures of the Antarctic ozone hole in Southern Hemisphere surface climate change, Nature Geosci., 4, 741–749, https://doi.org/10.1038/ngeo1296, 2011.

Toggweiler, J.: Variation of atmospheric CO_2 by ventilation of the ocean's deepest water, Paleoceanography, 14, 571–588, 1999.

Tsujino, H., Urakawa, S., Nakano, H., Small, R. J., Kim, W. M., Yeager, S. G., Danabasoglu, G., Suzuki, T., Bamber, J. L., Bentsen, M., Böning, C. W., Bozec, A., Chassignet, E. P., Curchitser, E., Boeira Dias, F., Durack, P. J., Griffies, S. M., Harada, Y., Ilicak, M., Josey, S. A., Kobayashi, C., Kobayashi, S., Komuro, Y., Large, W. G., Le Sommer, J., Marsland, S. J., Masina, S., Scheinert, M., Tomita, H., Valdivieso, M., and Yamazaki, D.: JRA-55 based surface dataset for driving ocean–sea-ice models (JRA55-do), Ocean Modelling, 130, 79–139, https://doi.org/10.1016/j.ocemod.2018.07.002, 2018.

Völker, C. and Köhler, P.: Responses of ocean circulation and carbon cycle to changes in the position of the Southern Hemisphere westerlies at Last Glacial Maximum, Paleoceanography, 28, 726–739, https://doi.org/10.1002/2013PA002556, 2013.

Wanninkhof, R.: Relationship between gas exhange and wind speed over the ocean, Journal of Geophysical Research, 97, 7373–7381, 1992.

Waugh, D. W. and Haine, T. W. N.: How Rapidly Do the Southern Subtropical Oceans Respond to Wind Stress Changes?, Journal of Geophysical Research: Oceans, 125, e2020JC016 236, https://doi.org/10.1029/2020JC016236, e2020JC016236 2020JC016236, 2020.

Waugh, D. W., Banerjee, A., Fyfe, J. C., and Polvani, L. M.: Contrasting Recent Trends in Southern Hemisphere Westerlies Across Different Ocean Basins, Geophysical Research Letters, 47, e2020GL088 890, https://doi.org/10.1029/2020GL088890, 2020.

Ziehn, T., Chamberlain, M. A., Law, R. M., Lenton, A., Bodman, R. W., Dix, M., Stevens, L., Wang, Y.-P., and Srbinovsky, J.: The Australian Earth System Model: ACCESS-ESM1.5, Journal of Southern Hemisphere Earth Systems Science, https://doi.org/10.1071/ES19035, 2020.

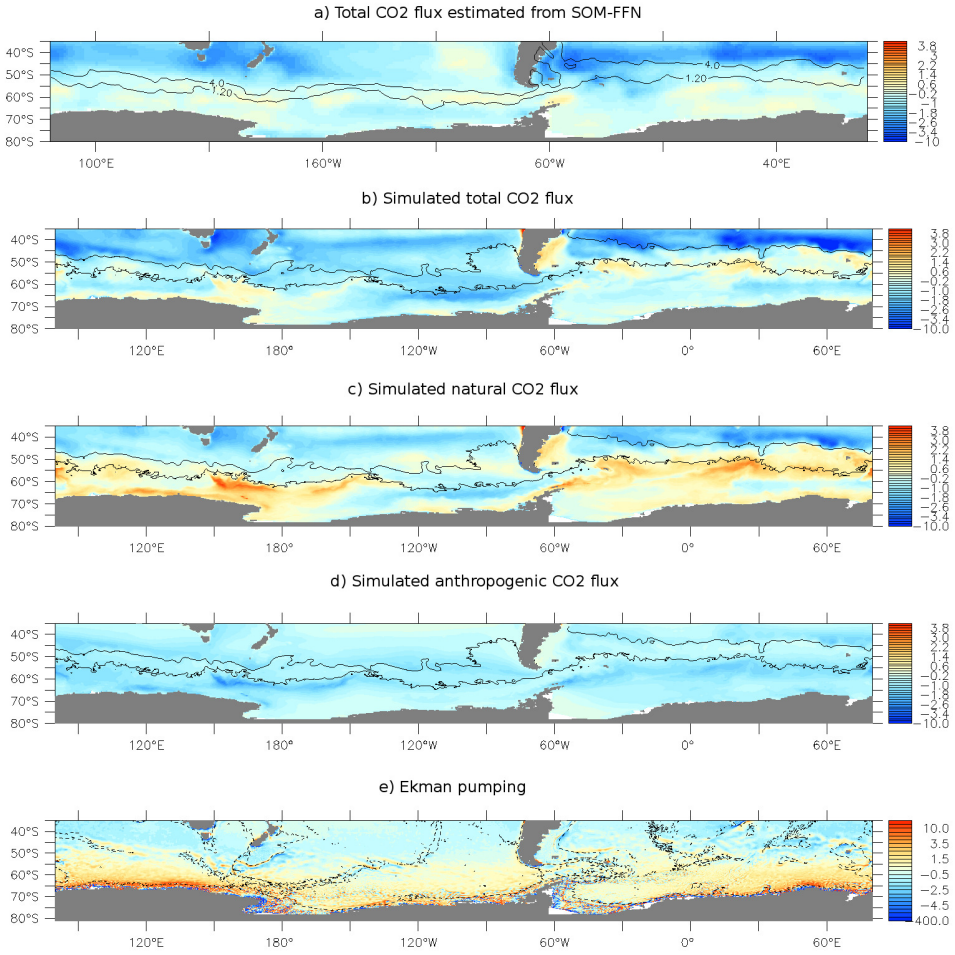

Figure 1. a) Total ocean to atmosphere CO_2 flux (molC/m^2/yr) as estimated from the SOM-FFN for the period 1982-2021 ~~(Landschützer et al., 2015)~~(Landschützer et al., 2016, 2020). The black contours indicate (from south to north) the northern edges of the polar front (PF) and the sub-Antarctic front (SAF) using the definition of Sokolov and Rintoul (2009) and the temperature data from the World Ocean Atlas (Locarnini et al., 2013). Simulated b) Total, c) natural and d) anthropogenic ocean to atmosphere CO_2 flux (molC/m^2/yr) averaged over the period 1982-2021 in the 0.1° ACCESS-OM2-01. The black contours indicate ~~(from south to north)~~ the northern edges of the PF and SAF using the definition of Sokolov and Rintoul (2009). e) Ekman pumping (x10^{-6} m/s) averaged over the period 1982-2021 in the numerical experiment. The black lines overlaid represent the 2500m depth bathymetry contour.

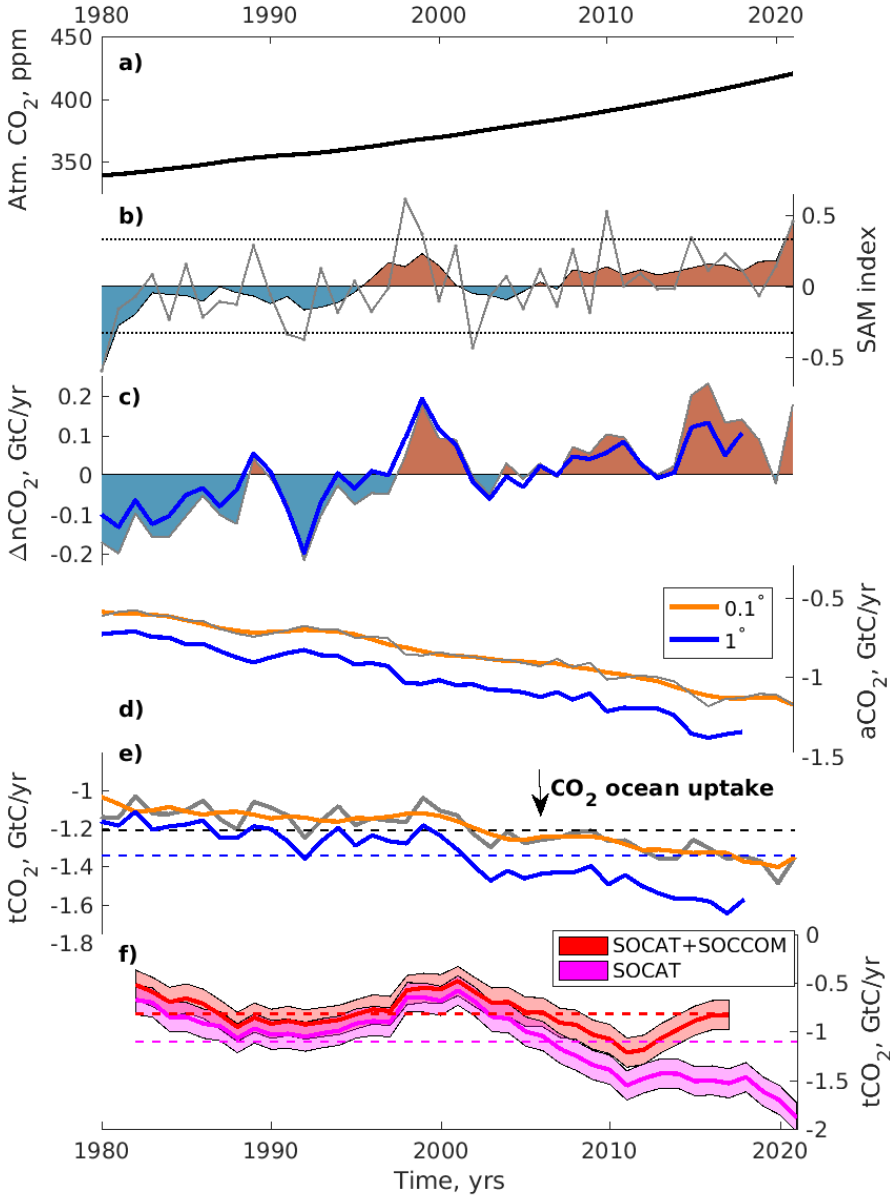

Figure 2. Time series of a) annual mean atmospheric CO_2 ~~growth rate (ppm/yr)~~ concentration used as forcing, b) SAM index calculated from the JRA55-do dataset (Stewart et al., 2020)~~, simulated~~. The horizontal dotted lines represent the thresholds used to define positive and negative SAM in the composites. Simulated integrated ocean to atmosphere ~~integrated c) nCO~~CO_2 ~~anomalies with respect to~~ fluxes in the ~~1970-2021~~ ACCESS-OM2-01 (0.1°, annual mean in grey and 5-yr running mean in orange) and ACCESS-OM2 (1°, ~~d~~annual mean in blue) ~~aCO~~simulations: c) nCO_2, ~~e~~d) ~~detrended~~ aCO_2~~anomalies with respect to the 1970-2021 mean~~, ~~f) tCO_2~~ and ~~g~~e) ~~detrended~~ tCO_2~~anomalies with respect to the 1970-2021 mean~~. ~~h~~f) SO tCO_2 flux ~~(GtC/yr)~~ as derived from the SOM-FFN ~~(Landschützer et al., 2019; Bushinsky et al., 2019)~~(red) including both the SOCAT and SOCCOM data (Bushinsky et al., 2019), and (magenta) only including the SOCAT data (Landschützer et al., 2020). The shading represents an uncertainty of 0.15 GtC/yr. All the CO_2 fluxes are integrated over the SO (35°S-80°S) and are in GtC/yr. ~~Light lines represent annual mean values, thick lines represent the 5-yr running means, and dashed~~ Dashed horizontal lines represent the mean over 1980-2021 or over the available period ~~For the SAM index, the~~

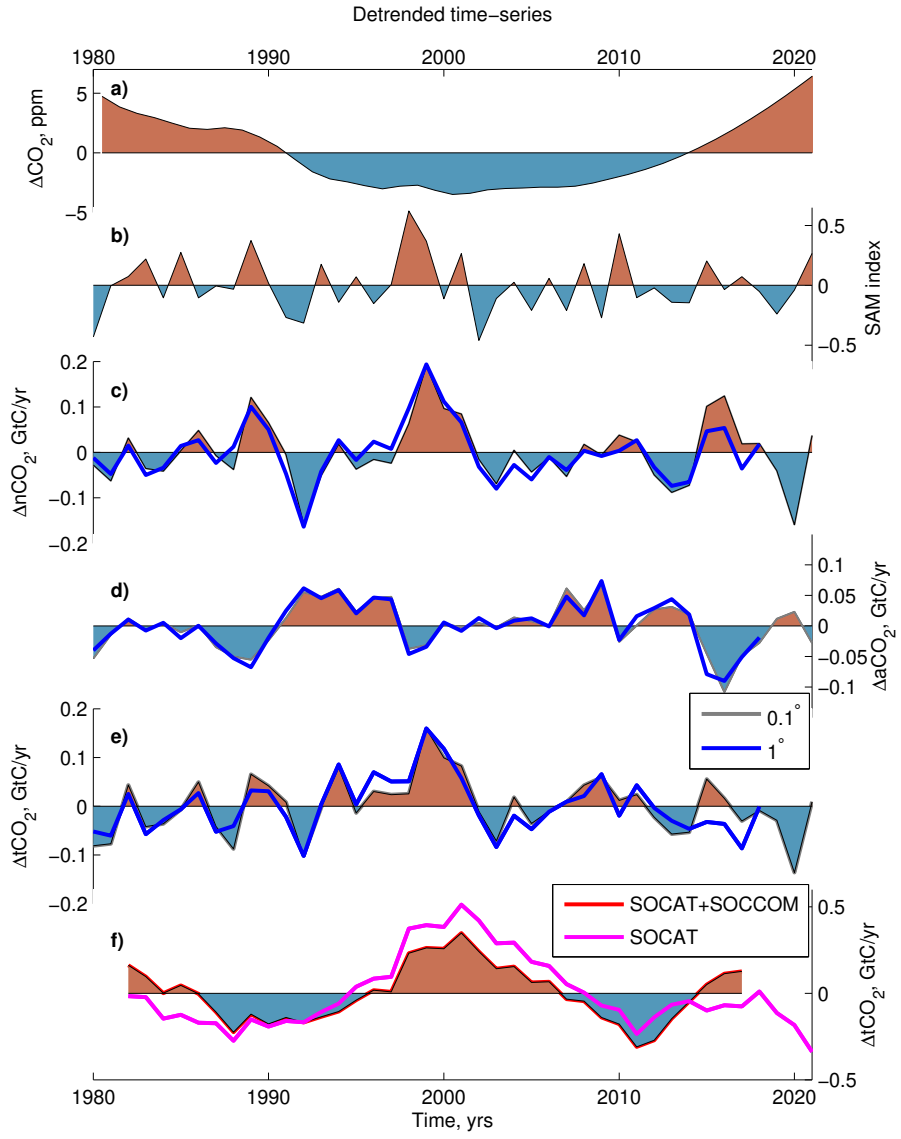

Figure 3. Detrended annual mean time series of a) ~~Non thermal~~ atmospheric CO_2 (~~blue~~ppm) ~~and thermal (cyan~~used as forcing, b) ~~pCO~~SAM index calculated from the JRA55-do dataset (Stewart et al., 2020). Detrended annual-mean simulated integrated ocean to atmosphere annual mean detrended CO_2 ~~contributions anomalies~~ fluxes in the ACCESS-OM2-01 ~~(ppm) south of 50~~0.1°~~S~~, grey, with light blue and ~~b) maximum zonal wind stress~~ red shadings indicating positive and negative anomalies ~~(N/m^2)~~ with respect to the ~~1980-1982~~ mean~~over~~) and the ~~Atlantic sector~~ ACCESS-OM2 (~~70~~1°~~W-20°E~~, blue) ~~. c-d~~simulations: c) ~~Same as a-b~~nCO_2, d) ~~for the Indian sector (20°E-130°E~~aCO_2, e) tCO_2. ~~e-f~~f) ~~Same~~ Detrended SO tCO_2 flux as ~~a-b~~derived from the SOM-FFN including both the SOCAT and SOCCOM data (red) ~~for~~ (Bushinsky et al., 2019), and including the ~~Pacific sector~~ SOCAT data only (~~130°E-70°W~~magenta) (Landschützer et al., 2020). ~~The correlation coefficients between~~ All the ~~non-thermal pCO~~CO_2 ~~variations and~~ fluxes are integrated over the ~~wind stress changes~~ SO (35°S-80°S) and are ~~indicated for each sector~~in GtC/yr.

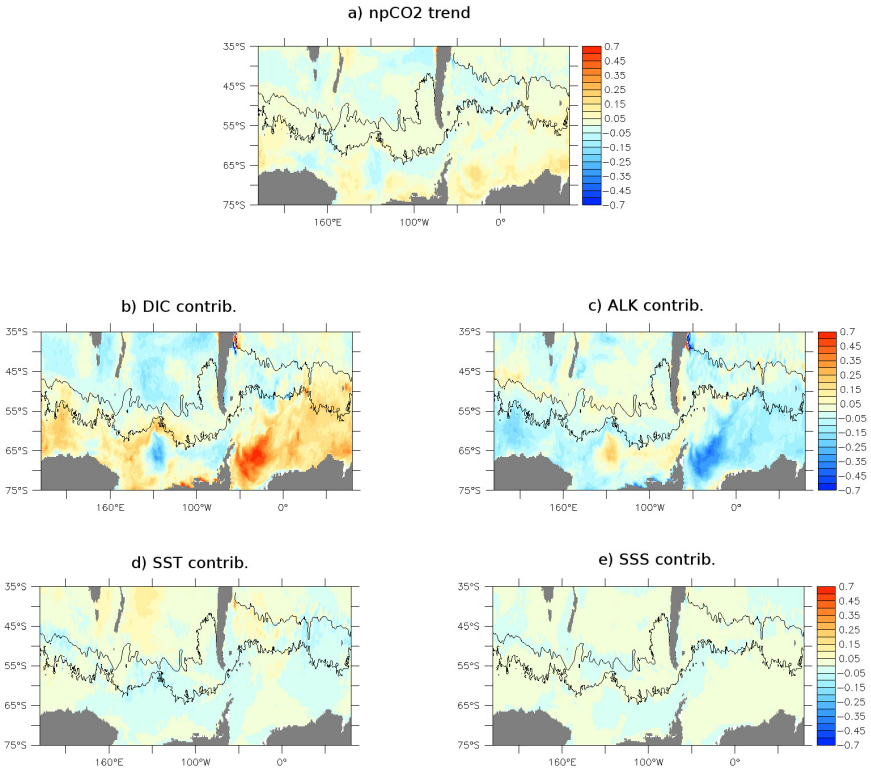

Figure 4. a) Natural pCO_2 trend (ppm/decade) between 1981 and 2021 and b) nDIC, c) ALK, d) SST and e) SSS contributions to the natural pCO_2 trend (ppm/decade) for the ACCESS-OM2-01 simulation.

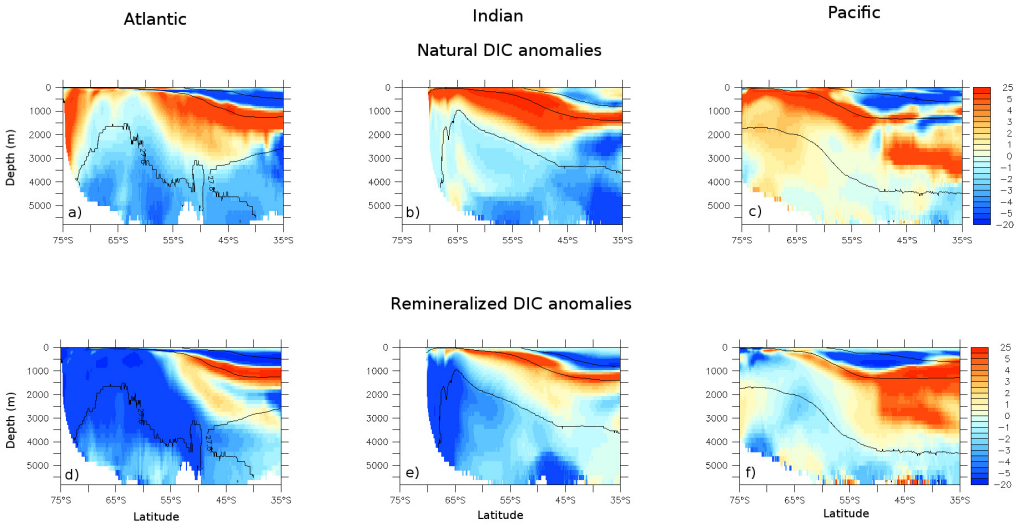

Figure 5. Zonally averaged (a-c) natural DIC, and (d-f) remineralized DIC (mmol/m^3) averaged over (left) the Atlantic, (middle) the Indian and (right) the Pacific for years 2017-2021 compared to 1980-1982 for the ACCESS-OM2-01 simulation. The density of the AABW (≥1028.31 kg/m^3), the AAIW (1027.5≥AAIW≥1026.95 kg/m^3) and the SAMW (≤1026.95 kg/m^3) are overlaid.

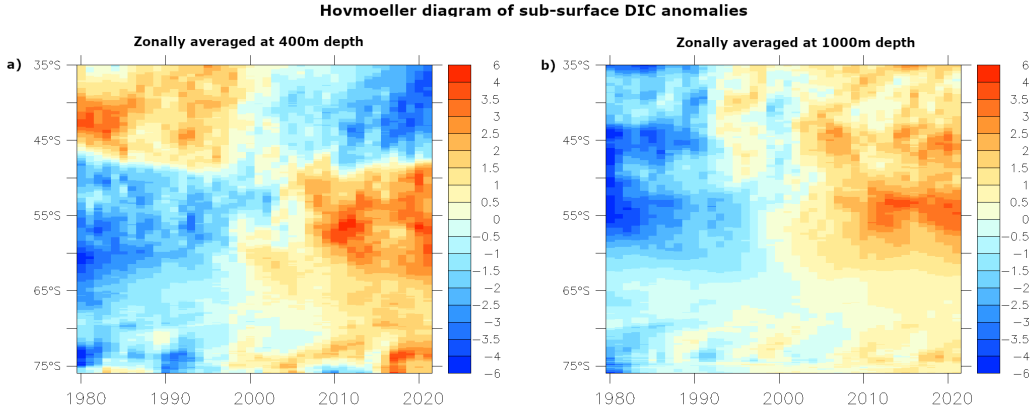

Figure 6. Hovmoeller diagram over the period 1980-2021 of zonally averaged nDIC anomalies (mmol/m^3) as a function of time and latitude at a) 400 m and b) 1000 m depth compared to the time average nDIC in the ACCESS-OM2-01 simulation.

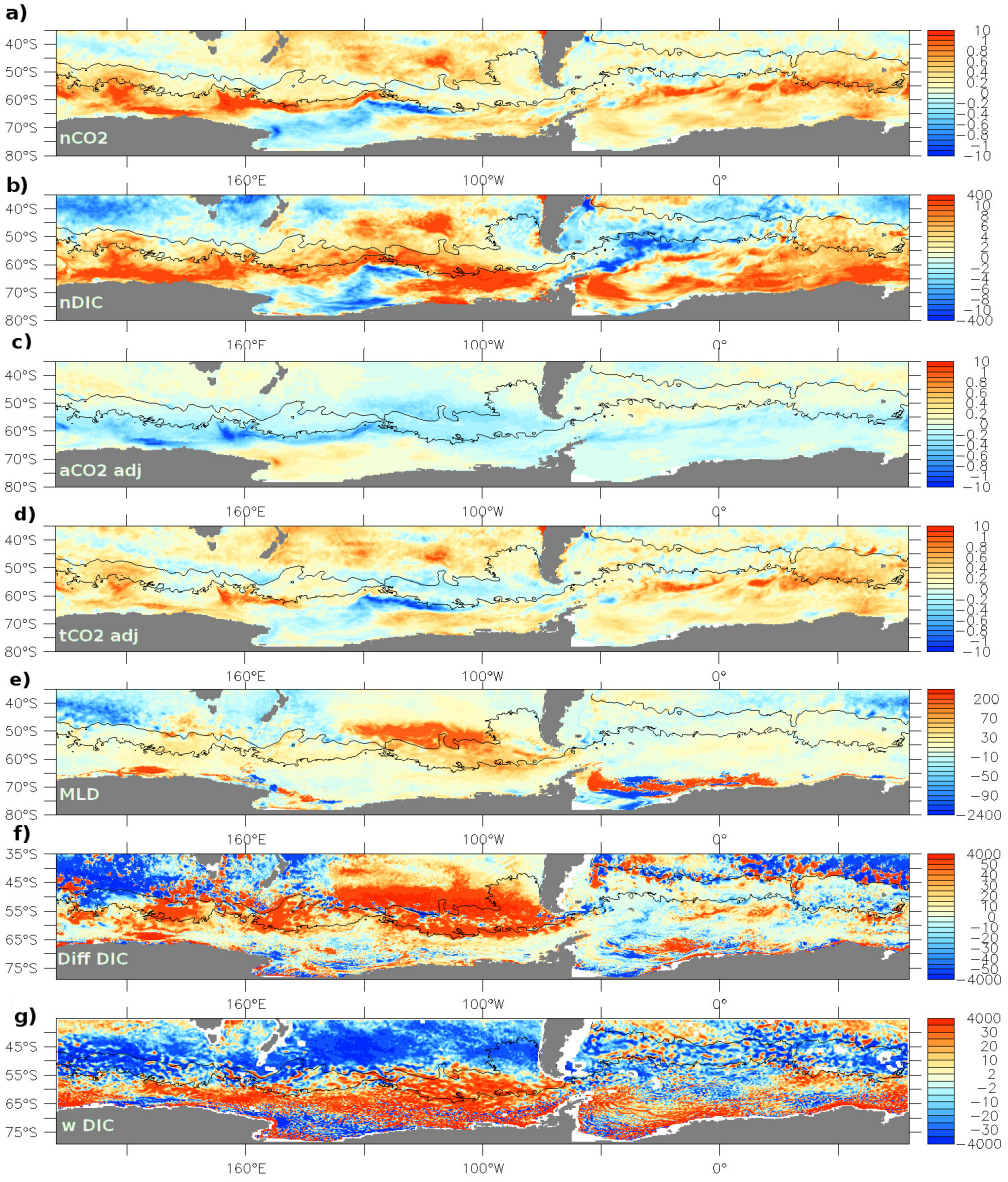

Figure 7. a) nCO_2 flux (mol/m^2/yr), b) surface nDIC (mmol/m^3), c) adjusted aCO_2 flux (~~mol~~molC/m^2/yr) and d) adjusted tCO_2 flux (~~mol~~molC/m^2/yr) anomalies for a composite of positive phases of the SAM (≥~~0.83~~0.33, i.e. 1998, 1999, 2010, 2015 and 2021) compared to a composite of negative SAM years (≤0.33, i.e. 1980, 1991, 1992, 2002) for the ACCESS-OM2-01 simulation. Linear trends in aCO_2 fluxes have been removed from the aCO_2 and tCO_2 anomalies to take into account the difference in mean years between the composite of positive and negative SAM years. Annual average anomalies of e) maximum monthly mixed layer depth (m), f) vertical diffusivity multiplied by the DIC gradient at the base of mixed layer (~~mol~~molC/m^2/yr) and g) vertical Ekman DIC advection with a 21 point spatial smoothing (~~mol~~molC/m^2/yr), for positive phases of the SAM compared to negative SAM years.

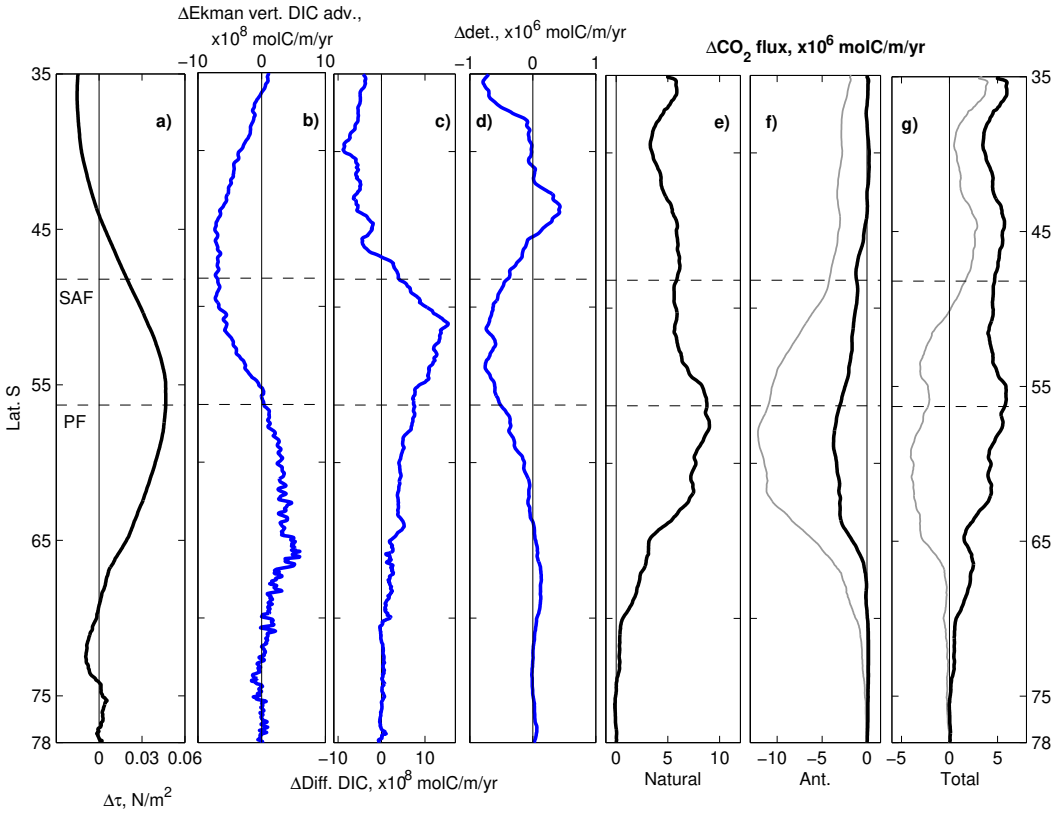

Figure 8. a) Zonally averaged wind stress anomalies (N/m^2); Anomalies in zonally integrated b) vertical Ekman DIC advection (x10^8 ~~mol~~molC/m/yr), c) vertical diffusivity multiplied by the DIC gradient at the base of mixed layer (x10^8 ~~mol~~molC/m/yr), d) detritus flux at 100m depth (x10^6 ~~mol~~molC/m/yr), e) nCO_2, f) aCO_2 and g) tCO_2 ~~total~~ fluxes (x10^6 molC/m/yr) for the positive SAM composite compared to the negative SAM composite in the ACCESS-OM2-01 simulation. In f and g) the grey lines represent the ~~actual data~~ simulated aCO_2 and tCO_2 fields while the black lines include a correction for the fact that the positive SAM composite represents more recent years than the negative SAM composite. The linear trends in aCO_2 and tCO_2 fluxes between 1980 and 2021 are calculated. The equivalent mean aCO_2 and tCO_2 flux differences between the mean positive and negative SAM composites are then subtracted.

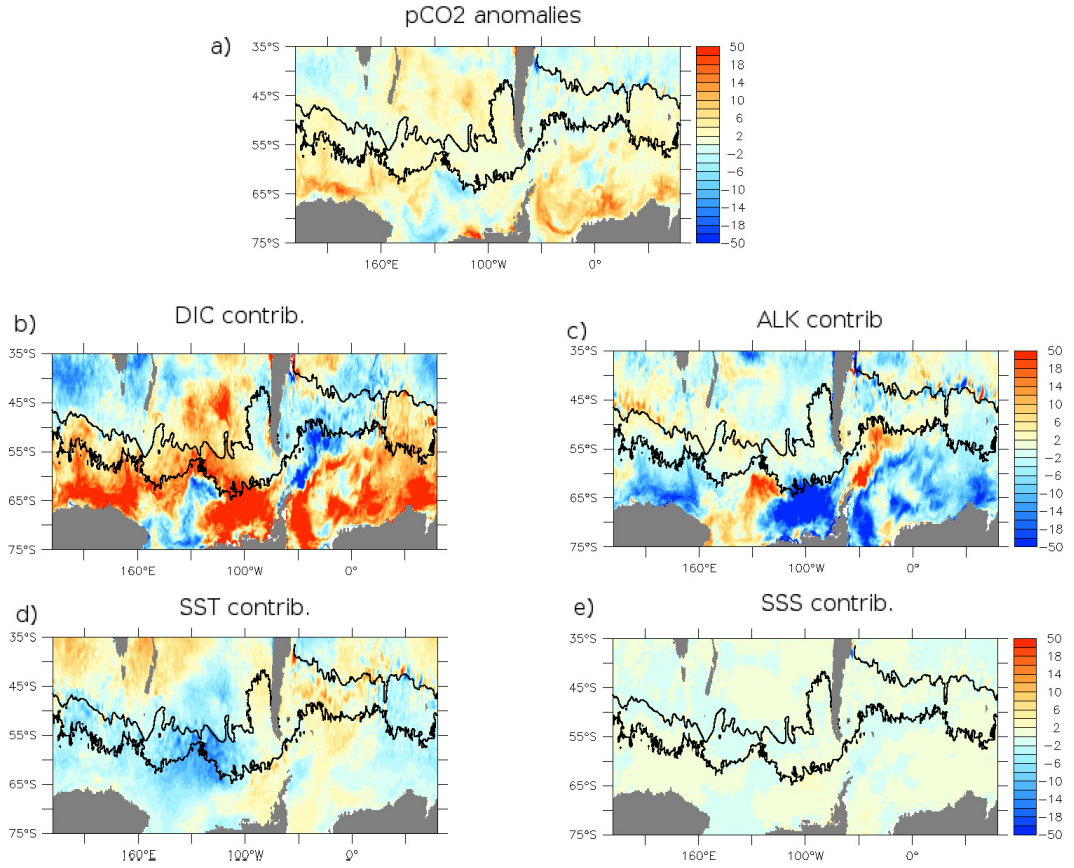

Figure 9. Surface ocean a) natural pCO_2 anomalies (ppm) for a composite of positive phases of the SAM compared to a composite of negative SAM years (see Fig. 7) and the pCO_2 contributions (ppm) from b) ~~DIC~~nDIC, c) ALK, d) SST and e) SSS for the ACCESS-OM2-01 simulation.

~~Zonally averaged (a-c) dissolved O_2 (mmol/m^3), (d-f) natural DIC, (g-i) anthropogenic DIC and (j-l) total DIC anomalies (mmol/m^3) averaged over (left) the Atlantic, (middle) the Indian and (right) the Pacific for years 2017-2021 compared to 1980-1982. The density of the AABW ($\geq$1028.31 kg/m^3), the AAIW (1027.5$\geq$AAIW$\geq$1026.95 kg/m^3) and the SAMW ($\leq$1026.95 kg/m^3) are overlaid. For anthropogenic DIC, the anomalies represent the deviation from the linear accumulation of anthropogenic DIC following the pattern obtained during the 1970s Gruber et al. (2019a). The total DIC anomalies represent the sum of the natural and anthropogenic DIC anomalies.~~

~~Hovmoeller diagram of zonally averaged nDIC anomalies (mmol/m^3) as a function of time and latitude at a) 400 m and b) 1000 m depth compared to the time average nDIC.~~